*J. Fluid Mech.* (2024), *vol*. 998, A46, doi:10.1017/jfm.2024.800

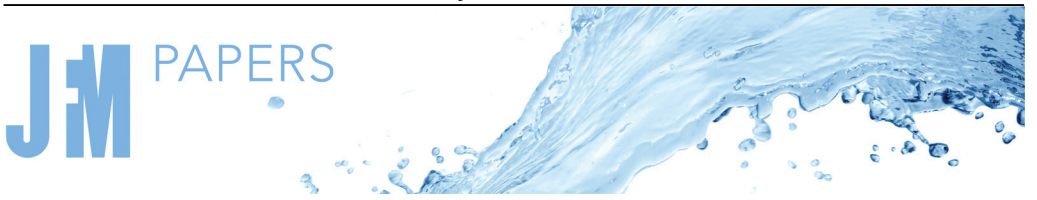

# Predicting bifurcation and amplitude death characteristics of thermoacoustic instabilities from PINNs-derived van der Pol oscillators

**Mingke Xie[1,2], Xinyu Zhao[1], Dan Zhao[1,†], Jianqin Fu[2,†], Cody Shelton[3] and Bernhard Semlitsch[4]**

[1]Department of Mechanical Engineering, Faculty of Engineering, University of Canterbury, Christchurch 8140, New Zealand

[2]State Key Laboratory of Advanced Design and Manufacturing for Vehicle Body, Hunan University, Changsha 410082, PR China

[3]Department of Aerospace Engineering, Auburn University, 211 Davis Hall, Auburn, AL 36849-5338, USA

[4]Institute of Energy Systems and Thermodynamics, TU Wien, Getreidemarkt 9, Vienna 1060, Austria

(Received 12 December 2023; revised 18 June 2024; accepted 9 July 2024)

Self-sustained thermoacoustic oscillations as observed in low-emission combustion-involved gas turbines and aero-engines involve complicated thermal fluid–acoustics interaction and rich nonlinear dynamics. Such pulsating oscillations are known as thermoacoustic instability. When it occurs, large-amplitude limit cycle oscillations (LCOs) of thermodynamic parameters are frequently observed. These LCOs could cause overheating, flame flashback, and even engine failures. Thus it is critical to understand and predict the generation mechanisms and nonlinear dynamics behaviours, and then develop corresponding control approaches to prevent or control the onset of such instabilities. In this work, we develop and extend the classical van der Pol oscillators by integrating a physics-informed neural networks (PINNs) algorithm with a modelled nonlinear Rijke-type thermoacoustic combustor. The theoretical Rijke tube system (with Galerkin expansion and modified King's law implemented) and a CFD simulation model are applied to provide 'training/calibration data' for the extended van der Pol (EVDP)-PINNs model. The optimized EVDP oscillators are confirmed to be capable of capturing the key nonlinear characteristics by comparing the transient growth behaviours of thermodynamic perturbations and LCO amplitude and frequency. Further investigations are conducted to obtain Hopf bifurcation and amplitude death (AD) characteristics. Comparison is then made to the coupled EVDP systems. Quite similar Hopf bifurcation features, but

† Email addresses for correspondence: dan.zhao@canterbury.ac.nz, fujianqin@hnu.edu.cn

differences in regions of AD, are observed. In general, we demonstrate an applicable approach to intelligently 'learn' a nonlinear thermoacoustic system and to create reliable EVDP oscillator systems, which have great potential to contribute to the development and testing of control approaches, such as the coupling described in this work, which may replace costly experimental tests.

**Key words:** aeroacoustics, noise control, nonlinear instability

## 1. Introduction

Thermoacoustic instabilities are self-sustained oscillations (Balasubramanian & Sujith 2008; Liu, Cheng & Du 2022) where acoustic waves and unsteady heat release compose a positive feedback loop (Bragg 1964; Dowling 1995; Lyu, Fang & Wang 2023). These fluctuations can become intense and cause performance degradation, emission deterioration (Zhang *et al.* 2023), severe noise (Su, Yang & Morgans 2022), lifespan reduction, structural damage, and even catastrophic machine failure in propulsive systems or power generation units. Thus acquiring control methods to prevent or restrict such undesirable high-amplitude oscillations of the self-excited system is of great significance (Juniper & Sujith 2018; Sun *et al.* 2022).

Many studies (Dowling & Morgans 2005; Zhao & Li 2015; Guan *et al.* 2023) have underlined the importance of suppressing pressure oscillations. Passive control methods, such as perforated liners, baffles, and half- and quarter-wave tubes, have been employed to dissipate pressure fluctuations effectively (Zhao & Morgans 2009; Zhao 2023*b*). Active control (Zhang *et al.* 2020; Naji *et al.* 2023), such as feedback control (Zhao & Reyhanoglu 2014), open (Wu *et al.* 2019) or close-loop active control (McManus, Poinsot & Candel 1993; Zhao 2023*a*), and adaptive control (Zhao 2023*a*), can suppress undesired instabilities through activatable devices. Their practical implementation is limited by the installation of feedback devices (Balusamy *et al.* 2015; Biwa *et al.* 2016). Therefore, a recently proposed approach, which controls pressure oscillations in coupled systems, attracted the authors' attention. Based on the amplitude death (AD) theory, which has been validated against experiments (Zhao *et al.* 2015; Sahay *et al.* 2021), coupling two systems using a needle valve and a vinyl tube can entirely suppress the unwanted oscillations (Biwa, Tozuka & Yazaki 2015; Thomas *et al.* 2018; Srikanth *et al.* 2022). For the design of coupled systems, the description of the non-normality and nonlinearity characteristics (Yang, Pang & Li 2021; Wu *et al.* 2023) by partial differential equations (PDEs) is essential. However, the complexity of engineering systems challenges the derivation of PDEs for such applications.

The van der Pol (VDP) equation is a reliable alternative to formulate deterministic system descriptions, which has been studied extensively (Nbendjo & Yamapi 2007; Yamapi, Nana Nbendjo & Kadji 2007; Vinod & Balaram 2023) owing to its capacity to mimic the nonlinear thermoacoustic instability behaviour on account of its adherence to the Liénard theorem (Perko 2013). According to Guan *et al.* (2021), the low-order oscillator model consisting of two simple VDP oscillators can reproduce many synchronization phenomena, including AD characteristics. Next, once the VDP equation is established, the unknown parameters need to be determined from the available data. The recently developed physics-informed neural networks (PINNs) model solves PDEs via deep learning (Raissi, Perdikaris & Karniadakis 2017*a*,*b*; Lu *et al.* 2021; Wang *et al.* 2023), and has been applied to fluid mechanics and thermoacoustics problems (Mariappan, Nath

& Karniadakis 2023; Ozan & Magri 2023). Thereby, novel perspectives opened up to determine the unknown parameters of inverse problems. That is, incomplete PDEs can be predicted using relatively few experimental measurements (Aliakbari *et al.* 2023; Xu *et al.* 2023) to replace prohibitively expensive methods in inverse flow problems (Cai *et al.* 2021).

The horizontal Rijke tube is a simplistic and thermoacoustic unstable system where PDEs can describe its behaviour. On the contrary, the thermoacoustic behaviour of engineering systems – e.g. thermoacoustic engines (TAEs), afterburners, Ramjet engines, and rocket motors – can be assessed only by experimental measurements. The derivation of specific PDEs for controlling strategy estimation of such complex systems is impossible. Thus we present a methodology based on the PINNs algorithm to determine a system instability behaviour by precise differential equations. The proposed extended VDP (EVDP)-PINNs method is validated against theoretical and simulation data, exhibiting acceptable errors. Additionally, the Hopf bifurcation and AD characteristics of the coupled EVDP systems are computed and compared with the coupled theoretical Rijke tube systems. Thereby, the physical significance of the EVDP system in the field of thermoacoustics is shown. Combining the results of the averaging method and the generalized scaling method with the AD boundary analysis provides each term in the EVDP system with a physical significance.

## 2. Methods

### 2.1. *The EVDP system*

The dimensionless pressure perturbation of a combustion system, as plotted in figure 1(*a*), exhibits a pronounced non-normal system behaviour, where a high-amplitude limit cycle establishes from an initially small perturbation. To replicate such system characteristics, the VDP equation is selected (Nbendjo & Yamapi 2007; Yamapi *et al.* 2007; Vinod & Balaram 2023). The non-conservative oscillator with nonlinear damping can be written in its basic form without source term as

$$\ddot{\psi} - \mu(1 - \psi^2)\dot{\psi} + \psi = 0, \tag{2.1}$$

where $\psi$ is the investigated quantity, the dot over the variable represents the temporal derivative, and $\mu$ is a parameter defining the nonlinearity and damping strength. The classical VDP oscillator with $\mu = 0.2$ resembles the dimensionless pressure perturbation as shown in figure 1, proving that the classical VDP equation can mimic the behaviour of combustion system instabilities.

To enhance the applicability of the classical VDP equation to thermoacoustic instabilities, we decompose the first-order differential term and add a time scaling parameter $\mu_3$ to reformulate (2.1) into

$$\ddot{\psi} - \mu_1\mu_3\dot{\psi} + \mu_2\mu_3\psi^2\dot{\psi} + \mu_3^2\psi = 0. \tag{2.2}$$

Equation (2.2) still satisfies the properties of the Liénard theorem, providing a unique and stable limit cycle. Observing the shape of the oscillation depicted in figure 1, the fundamental characteristics are the time required for the initial perturbation to evolve into a limit cycle, and the resulting limit cycle amplitude. Figure 2 visualizes the extension of the parameter space, introducing further parameters, thereby improving the expressive capacity compared to the one-dimensional diagonal line ($\mu_1 = \mu_2$).

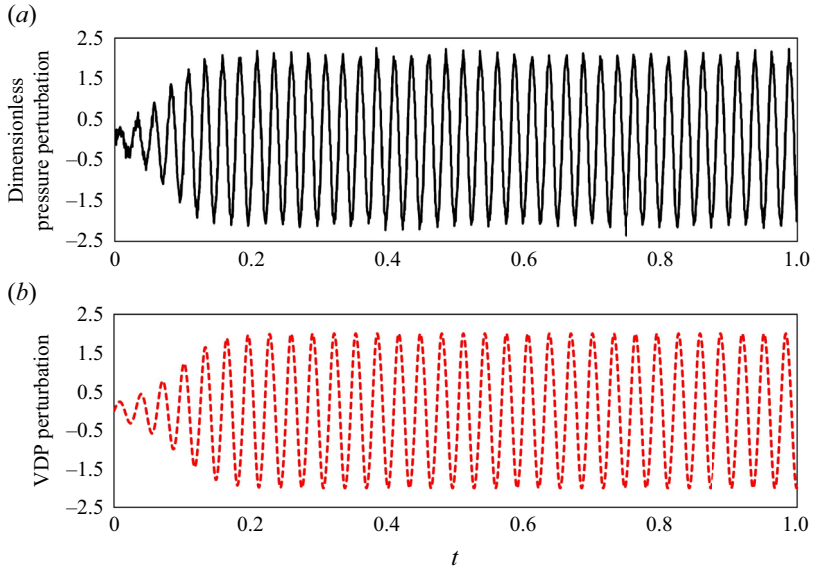


Figure 1. Instability of a combustion system obtained (*a*) experimentally (Li *et al.* 2016*a*) and (*b*) with the classical VDP equation.

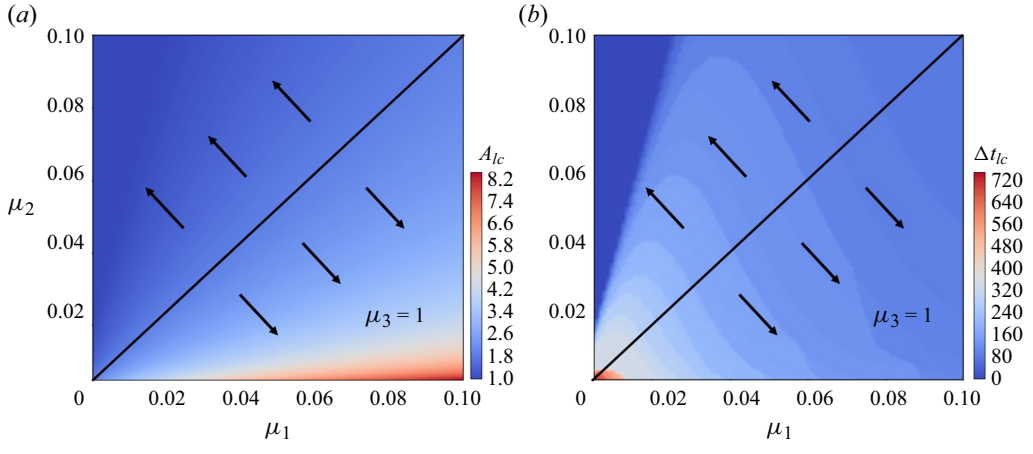


Figure 2. Contour plots of (*a*) the limit cycle amplitude ($A_{lc}$), and (*b*) the time duration to reach a limit cycle ($\Delta t_{lc}$, where the value zero indicates an unexcited oscillator).

To further characterize the dynamics described in (2.2), the Krylov–Bogolyubov method of averaging is applied (Krylov & Bogolyubov 1947; Nayfeh 2000). Therefore, (2.2) is rewritten as

$$\ddot{\psi} + \mu_3^2 \psi = \varepsilon_a \mu_3 \dot{\psi}(\mu_1 - \mu_2 \psi^2). \tag{2.3}$$

Here, $\varepsilon_a$ is introduced as a placeholder with a small value to facilitate the averaging procedure. Making this assumption implies weak nonlinearity (small $\mu_1$ and $\mu_2$), causing the oscillator to behave as one undergoing sinusoidal oscillations, which is common for thermoacoustic applications. Therefore, this solution is valid only in the region where $\mu_1$ and $\mu_2$ are small, a condition utilized throughout this paper. In fact, setting $\mu_1 = \mu_2 = \varepsilon_a$

and $\mu_3 = 1$ recovers the classical VDP oscillator. Proceeding, the solution is assumed to have the form

$$\psi(t) = a(t)\cos\big(\mu_3 t + \theta(t)\big), \tag{2.4}$$

where $a(t)$ and $\theta(t)$ are time-varying. However, they vary slowly compared to the period of oscillations due to the assumption made previously on $\varepsilon_a$ in (2.3). This leads to the following two equations for the amplitude and phase responses, respectively:

$$\frac{\mathrm{d}a}{\mathrm{d}t} = -\frac{\varepsilon_a}{2\mu_3} F(a) \tag{2.5}$$

and

$$\frac{\mathrm{d}\theta}{\mathrm{d}t} = -\frac{\varepsilon_a}{2a\mu_3} G(a), \tag{2.6}$$

where $F(a)$ and $G(a)$ represent coefficients of the Fourier expansion of the right-hand side of (2.3). They can be expressed as

$$F(a) = \tfrac{1}{4}a(-4\mu_1 + a^2\mu_2)\mu_3^2 \tag{2.7}$$

and

$$G(a) = 0. \tag{2.8}$$

As a result, the phase remains constant, and the amplitude is further described as

$$a(t) = \frac{2\exp(\frac{1}{2}\varepsilon_a\mu_1\mu_3 t)\sqrt{\mu_1}}{\sqrt{\dfrac{4\mu_1}{a_0^2} + \mu_2\big(\exp(\varepsilon_a\mu_1\mu_3 t) - 1\big)}}, \tag{2.9}$$

with the initial condition $a(0) = a_0$ already included. Using this equation for amplitude, we find the limit cycle oscillation as

$$\lim_{t\to\infty} a(t) = 2\frac{\sqrt{\mu_1}}{\sqrt{\mu_2}}. \tag{2.10}$$

This formulation has a remarkable resemblance to figure 2. It is apparent that a strong agreement with the numerical integration of (2.2) is obtained.

2.1.1. *The PINNs model for inverting a thermoacoustic oscillations problem*

Estimating unknown variables based on the experimental measurements or available data from theoretical models constitutes a typical inverse problem. Therefore, the PINNs algorithm for solving inverse problems is highly suitable for addressing this system generalization task, as outlined in figure 3. Here, the integration of PDEs and available data is accomplished seamlessly by incorporating new PDE loss terms into the loss function of the neural network (Yazdani *et al.* 2020; Karniadakis *et al.* 2021; Yu *et al.* 2022). As depicted in (2.11) below, the total loss consists of the supervised data loss and

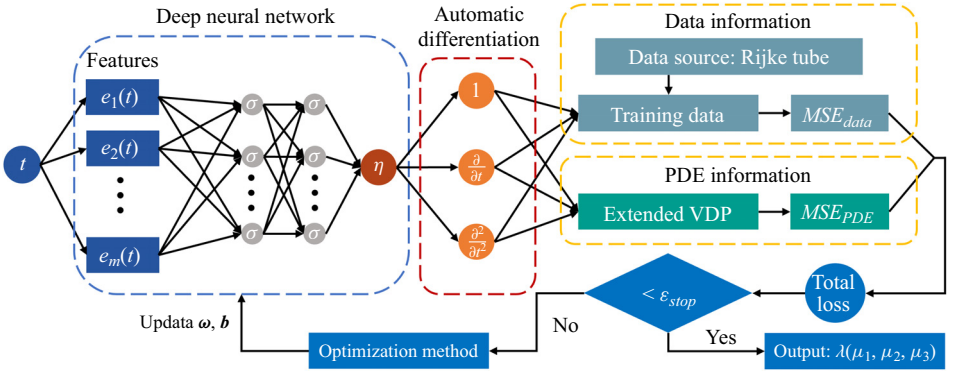


Figure 3. The PINNs architecture for the inverse thermoacoustic problem. Here, $MSE_{data}$ and $MSE_{PDE}$ represent the mean square error of the data and the PDE, respectively.

unsupervised PDEs loss (EVDP equation here):

$$L = \omega_{data} L_{data} + \omega_{PDE} L_{PDE}, \tag{2.11}$$

where

$$L_{data} = \frac{1}{N_{data}} \sum_{i=1}^{N_{data}} \left[\psi(t_i, \boldsymbol{\mu}) - \psi(t_i)\right]^2, \tag{2.12}$$

$$L_{PDE} = \frac{1}{N_{data}} \sum_{j=1}^{N_{data}} \left[\ddot{\psi}(t_j) - \mu_1\mu_3\, \dot{\psi}(t_j) + \mu_2\mu_3\, \psi^2(t_j)\, \dot{\psi}(t_j) + \mu_3^2\, \psi(t_j)\right]^2. \tag{2.13}$$

Here, $\omega_{data}$ and $\omega_{PDE}$ are the loss weights of the supervised loss $L_{data}$ and the unsupervised PDE loss $L_{PDE}$, respectively, $N_{data}$ represents the number of the training data, and $\psi(t_i)$ and $\psi(t_i, \boldsymbol{\mu})$ are the $i$th training node and its fitting value.

The neural network parameters and unknowns, $\boldsymbol{\mu}$ can be determined simultaneously by minimizing the loss function $L$ through a gradient-based optimizer (the Adam optimizer was applied in the present work). In the features layer, employing $m$ functions of the form $e(\cdot)$ to construct $m$ features $e(t)$ for specific solution patterns of the PDEs is efficient. Trigonometric functions are used due to the oscillation periodicity in this study. The training is performed using all the data (including the exponentially growing period and the saturating period) with default hyperparameters and learning rate $10^{-3}$. Additionally, a two-stage training strategy is employed to accelerate the network convergence, which involves initial training with only supervised losses, and further training considering all losses. The algorithm is implemented in Python using the open-source library DeepXDE (Lu *et al.* 2021). The unknown variables are acquired when stabilizing with the neural network time step.

### 2.2. *Thermoacoustic waves generation and propagation*

An analytically traceable system is selected to validate the aforementioned method's effectiveness in obtaining deterministic descriptions. Among various prototypical thermoacoustic systems, the horizontal Rijke tube with acoustically compact heat sources (Rayleigh 1878; Raun *et al.* 1993) is suitable and considered in this work. The heat release

is modelled by the modified King's law theory (Heckl 1990). The dimensionless governing equations are

$$\frac{\partial u}{\partial t} + \frac{\partial p}{\partial x} = 0, \tag{2.14}$$

$$\frac{\partial p}{\partial t} + \frac{\partial u}{\partial x} + \zeta p - \beta \left\{ \left| \frac{1}{3} + u_f(t - \tau_1) \right|^{1/2} \right\} \delta_D(x - x_f) = 0, \tag{2.15}$$

where the flow parameters $u$, $p$ and $\rho$ represent the fluctuation components of velocity, pressure and density, respectively. Here, $\zeta$ is a damping coefficient, $\tau_1$ is a time delay between the velocity preoccupation and the heat source response, $x_f$ is the location of the hot wire, and $\delta_D$ is the Kronecker delta. Also, $\beta$ is the dimensionless heater power containing all hot-wire parameters:

$$\beta = \frac{1}{p_0\sqrt{u_0}} \frac{\gamma - 1}{\gamma} \frac{2L_w(T_w - T_0)}{S\sqrt{3}} \left( \pi \lambda_0 c_v \rho_0 \frac{d_w}{2} \right)^{1/2}, \tag{2.16}$$

where $L_w$, $d_w$ and $T_w$ represent the length, diameter and temperature of the hot wire, respectively. Here, $S$ is the cross-sectional area of the Rijke tube, $\lambda_0$ is the heat conductivity, $c_v$ is the specific isochoric heat capacity, and $\rho_0$, $p_0$, $u_0$ and $T_0$ are the density, pressure, velocity and temperature at the inlet.

Substituting the pressure perturbations expanded as a Galerkin series (Nagaraja, Kedia & Sujith 2009; Juniper 2011) into (2.14) gives

$$p = \sum_{n=1}^{N} \dot{\eta}_n(t)\, \varphi_n(x), \tag{2.17}$$

$$u = -\sum_{n=1}^{N} \eta_n(t)\, \varphi_n'(x), \tag{2.18}$$

where $N$ denotes the mode number, the overdot denotes the time derivative, the prime denotes the spatial derivative, and the functions $\varphi_n(x)$ are the eigensolutions of the homogeneous wave equation for the Rijke tube. Because the Rijke tube has pressure nodes at both ends, the mode shapes $\varphi_n(x)$ corresponding to the $n$th mode are illustrated as

$$\varphi_n(x) = \begin{cases} \sin\left( \dfrac{\omega_n L}{\bar{c}_1} x \right), & x \in [0, x_f], \\ \dfrac{\sin\left( \dfrac{\omega_n L}{\bar{c}_1} x_f \right)}{\sin\left( \dfrac{\omega_n L}{\bar{c}_2} x_f \right)} \sin\left[ \dfrac{\omega_n L}{\bar{c}_2} (1 - x) \right], & x \in [x_f, 1], \end{cases} \tag{2.19}$$

which satisfy the orthogonality condition. Here, $L$ is the length of the Rijke tube, and $\bar{c}_1$ and $\bar{c}_2$ are the speed of sound upstream and downstream of the hot wire. Substituting the

Galerkin expansion into (2.14) and (2.15) leads to

$$\frac{\mathrm{d}\dot{\eta}_n(t)}{\mathrm{d}t} + (\omega_n)^2\,\eta_n(t) + \zeta_n\,\dot{\eta}_n(t) = \frac{\beta}{E_n}\varphi_n(x_f)\left\{\left|\frac{1}{3} - \varphi_n'(x_f)\,\eta_n(t-\tau_1)\right|^{1/2} - \left(\frac{1}{3}\right)^{1/2}\right\}, \tag{2.20}$$

where $\omega_n$ are the eigenfrequencies calculated from the pressure and velocity continuity over the heat source (Backhaus & Swift 1999; Zhao & Reyhanoglu 2014; Karniadakis *et al.* 2021), $E_n$ are the integral constants (refer to the condition of orthogonality that is described mathematically in (32) of the previous work, Zhao 2012), and $\zeta_n$ are the damping coefficients (Nagaraja *et al.* 2009; Li *et al.* 2016*b*), accounting for all damping effects such as energy losses due to radiation, or viscous dissipation. The damping coefficient can be related to the eigenfrequency by

$$\zeta_n = \frac{1}{\pi}\,\omega_n\left(\xi_1\,\frac{\omega_n}{\omega_1} + \xi_2\sqrt{\frac{\omega_1}{\omega_n}}\right), \tag{2.21}$$

where $\xi_1$ and $\xi_2$ account for the energy losses due to radiation at the open ends as well as dissipation within the acoustic viscous and thermal boundary layers at the walls.

According to Bonciolini *et al.* (2021), only one dominant eigenmode is needed to approximate the system stability, including the limit cycle, although the unstable modes are coupled via nonlinear heat release rates. Thus the one-mode Galerkin expansion is employed in this study. The thermoacoustic Rijke tube system is represented by the coefficient values selected from previous studies (Backhaus & Swift 1999; Balasubramanian & Sujith 2008), which are listed in Appendix B. The initial conditions $[\eta(0), \eta'(0)]$ are assigned randomly, and kept consistent for the theoretical Rijke tube and EVDP system. As shown in figure 4, the system oscillations in terms of $\eta(t)$ and $\dot{\eta}(t)$ decay with low heater power or are excited to limit cycles (triggering) with high heater power. The Hopf bifurcation diagram in figure 4(*a*) shows that the limit cycle amplitude of the system behaves asymptotically as a function of $\beta$. Crossing the Hopf point ($\beta_{Hopf} = 1.17$) through the forward path, the system undergoes a Hopf bifurcation, which leads to an amplitude rise. In the reverse path, $\beta$ needs to be decreased significantly below the Hopf point to return the system to a stable state (known as the saddle point ($\beta_{saddle} = 1.01$). A typical subcritical bifurcation with a hysteresis region (bistable region) (Subramanian, Sujith & Wahi 2013; Biwa *et al.* 2015) is observed. In this region, the system can exhibit either a fixed stable point or a stable limit cycle, depending on the initial perturbations (Sujith & Unni 2020; Liu *et al.* 2023). These interpretations are consistent with previous studies (Thomas *et al.* 2018), indicating that the theoretical Rijke tube model generates reliable input data for the PINNs model to fit the unknown parameters of the EVDP equation.

Equation (2.20) can be rewritten for the first mode:

$$\frac{\mathrm{d}^2\eta(t)}{\mathrm{d}t^2} + \frac{\bar{\zeta}\omega}{\pi}\,\dot{\eta}(t) + \omega^2\,\eta(t) = \frac{\beta}{E}\,\varphi(x_f)\left\{\left|\frac{1}{3} - \varphi'(x_f)\,\eta(t-\tau_1)\right|^{1/2} - \left(\frac{1}{3}\right)^{1/2}\right\}. \tag{2.22}$$

An approximate solution may be found by applying the generalized scaling method (Nayfeh 2000). This method, related to the multiple scales technique, allows examination of both the amplitude response and the time scales of the problem. A small scaling

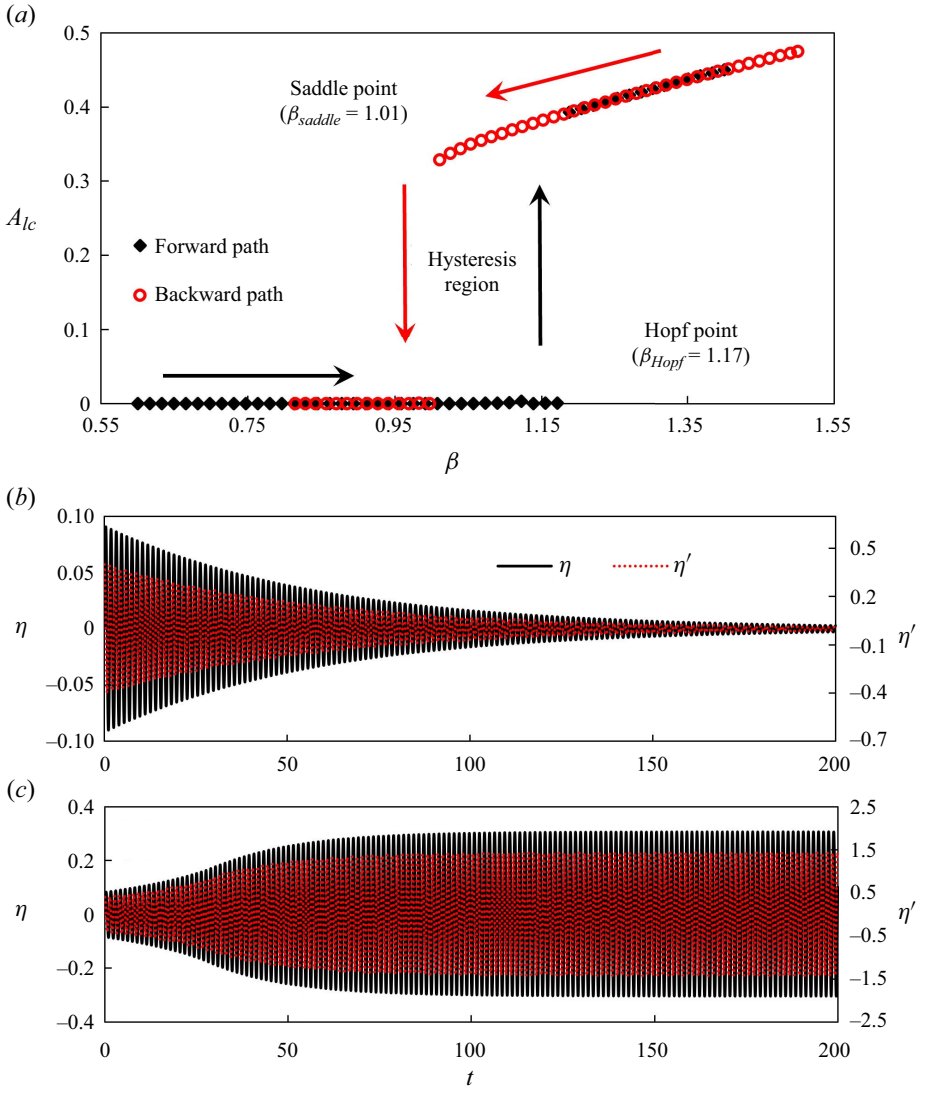


Figure 4. Rijke tube system. (*a*) Subcritical bifurcation diagram of the limit cycle amplitudes versus $\beta$. (*b*) Unexcited oscillation with small $\beta = 0.5$, AD – the amplitude tends to zero with time. (*c*) Excited oscillation with large $\beta = 2.1$, limit cycle oscillation – the amplitude tends to a non-zero stable value with time.

parameter $\varepsilon = 1/\omega$ is inserted into (2.20):

$$\varepsilon^2 \frac{\mathrm{d}^2\eta(t)}{\mathrm{d}t^2} + \varepsilon \frac{\bar{\zeta}}{\pi} \dot{\eta}(t) + \eta(t) = \varepsilon^2 \frac{\beta}{E} \varphi(x_f) \left\{ \left| \frac{1}{3} - \varphi'(x_f)\, \eta(t-\tau_1) \right|^{1/2} - \left(\frac{1}{3}\right)^{1/2} \right\}. \tag{2.23}$$

Although an approximate solution can be derived, it is quite cumbersome. Substituting the heat release term with an alternative formulation (Zhao *et al.* 2023) leads to

$$\varepsilon^2 \frac{\mathrm{d}^2\eta(t)}{\mathrm{d}t^2} + \varepsilon \frac{\bar{\zeta}}{\pi} \dot{\eta}(t) + \eta(t) = \varepsilon^2 K \varphi(x_f)\, \varphi'(x_f)\, (\eta - \tau_1 \dot{\eta}), \tag{2.24}$$

where $K$ is the heat correlation strength parameter. A time scale expansion is introduced with a slow and a fast time scale to aid the understanding of the underlying physics:

$$t_0 = t, \quad t_1 = \frac{g_0(t_0)}{\varepsilon} + g_1(t_0) + \varepsilon\, g_2(t_0) + \cdots, \tag{2.25a,b}$$

where $g_i$ will be determined through solvability conditions during the analysis. The temporal derivatives are also expanded:

$$\frac{\mathrm{d}}{\mathrm{d}t} = \frac{\partial}{\partial t_0}\frac{\mathrm{d}t_0}{\mathrm{d}t} + \frac{\partial}{\partial t_1}\frac{\mathrm{d}t_1}{\mathrm{d}t_0}\frac{\mathrm{d}t_0}{\mathrm{d}t} = \frac{\partial}{\partial t_0} + \left(\frac{g_0'}{\varepsilon} + g_1' + \varepsilon g_2' + \cdots\right)\frac{\partial}{\partial t_1} \tag{2.26}$$

and

$$\begin{aligned}\frac{\mathrm{d}^2}{\mathrm{d}t^2} = {} & \frac{\partial^2}{\partial t_0^2} + 2\left(\frac{g_0'}{\varepsilon} + g_1' + \varepsilon g_2' + \cdots\right)\frac{\partial^2}{\partial t_0\,\partial t_1} \\ & + \left(\frac{g_0''}{\varepsilon} + g_1'' + \varepsilon g_2'' + \cdots\right)\frac{\partial}{\partial t_1} + \left(\frac{g_0'}{\varepsilon} + g_1' + \varepsilon g_2' + \cdots\right)^2\frac{\partial^2}{\partial t_1^2}.\end{aligned} \tag{2.27}$$

Also, the time-varying coefficient $\eta$ can be expanded as a function of the two coordinates:

$$\eta = \eta_0(t_0, t_1) + \varepsilon\, \eta_1(t_0, t_1) + \varepsilon^2\, \eta_2(t_0, t_1) + \cdots. \tag{2.28}$$

Therefore, an approximate solution may be achieved with the relevant slow and fast time scale separation, which will aid in the understanding of the physics present. The three equations at different orders to be solved are given as

$$\left(g_0'\right)^2\frac{\partial^2\eta_0}{\partial t_1^2} + \frac{\bar{\zeta}}{\pi}\, g_0'\,\frac{\partial\eta_0}{\partial t_1} + \eta_0 = 0 \tag{2.29}$$

for the leading order,

$$\begin{aligned}&\left(g_0'\right)^2\frac{\partial^2\eta_1}{\partial t_1^2} + \frac{\bar{\zeta}}{\pi}\, g_0'\,\frac{\partial\eta_1}{\partial t_1} + \eta_1 + K\tau_1\,\varphi(x_f)\,\varphi'(x_f)\, g_0'\,\frac{\partial\eta_0}{\partial t_1} \\ &\quad + \frac{\bar{\zeta} g_1'}{\pi}\,\frac{\partial\eta_0}{\partial t_1} + g_0''\,\frac{\partial\eta_0}{\partial t_1} + 2g_0'g_1'\,\frac{\partial^2\eta_0}{\partial t_1^2} + \frac{\bar{\zeta}}{\pi}\,\frac{\partial\eta_0}{\partial t_0} + 2g_0'\,\frac{\partial^2\eta_0}{\partial t_1\,\partial t_0} = 0\end{aligned} \tag{2.30}$$

for the first order, and

$$\begin{aligned}&\left(g_0'\right)^2\frac{\partial^2\eta_2}{\partial t_1^2} + \frac{\bar{\zeta}}{\pi}\, g_0'\,\frac{\partial\eta_2}{\partial t_1} + \eta_2 - K\,\varphi(x_f)\,\varphi'(x_f)\,\eta_0 + \frac{\bar{\zeta} g_2'}{\pi}\,\frac{\partial\eta_0}{\partial t_1} + K\tau_1\,\varphi(x_f)\,\varphi'(x_f)\, g_1'\,\frac{\partial\eta_0}{\partial t_1} \\ &\quad + K\tau_1\,\varphi(x_f)\,\varphi'(x_f)\, g_0'\,\frac{\partial\eta_1}{\partial t_1} + g_1''\,\frac{\partial\eta_0}{\partial t_1} + \frac{\bar{\zeta} g_1'}{\pi}\,\frac{\partial\eta_1}{\partial t_1} + g_0''\,\frac{\partial\eta_1}{\partial t_1} \\ &\quad + \left(g_1'\right)^2\frac{\partial^2\eta_0}{\partial t_1^2} + 2g_0'g_2'\,\frac{\partial^2\eta_0}{\partial t_1^2} + 2g_0'g_1'\,\frac{\partial^2\eta_1}{\partial t_1^2} + \frac{\bar{\zeta}}{\pi}\,\frac{\partial\eta_1}{\partial t_0} + 2g_1'\,\frac{\partial^2\eta_0}{\partial t_1\,\partial t_0} \\ &\quad + 2g_0'\,\frac{\partial^2\eta_1}{\partial t_1\,\partial t_0} + \frac{\partial^2\eta_0}{\partial t_0^2} + K\,\varphi(x_f)\,\varphi'(x_f)\,\tau_1\,\frac{\partial\eta_0}{\partial t_0} = 0\end{aligned} \tag{2.31}$$

for the second order. As is typical with perturbation expansions, the homogeneous part of the equations has a common form, which can be described physically as a

damped oscillator. Equation (2.29) may be solved readily as

$$\eta_0(t_0, t_1) = A(t_0)\exp\left(\frac{-\bar{\zeta} - \sqrt{\bar{\zeta}^2 - 4\pi^2}}{2\pi\, g_0'(t_0)}\, t_1\right) + B(t_0)\exp\left(\frac{-\bar{\zeta} + \sqrt{\bar{\zeta}^2 - 4\pi^2}}{2\pi\, g_0'(t_0)}\, t_1\right). \tag{2.32}$$

As (2.30) and (2.31) have the same form as (2.29), the form of the homogeneous solution part should also be the same. Hence

$$\eta_1(t_0, t_1) = C(t_0)\exp\left(\frac{-\bar{\zeta} - \sqrt{\bar{\zeta}^2 - 4\pi^2}}{2\pi\, g_0'(t_0)}\, t_1\right) + D(t_0)\exp\left(\frac{-\bar{\zeta} + \sqrt{\bar{\zeta}^2 - 4\pi^2}}{2\pi\, g_0'(t_0)}\, t_1\right) \tag{2.33}$$

and

$$\eta_2(t_0, t_1) = E(t_0)\exp\left(\frac{-\bar{\zeta} - \sqrt{\bar{\zeta}^2 - 4\pi^2}}{2\pi\, g_0'(t_0)}\, t_1\right) + F(t_0)\exp\left(\frac{-\bar{\zeta} + \sqrt{\bar{\zeta}^2 - 4\pi^2}}{2\pi\, g_0'(t_0)}\, t_1\right). \tag{2.34}$$

The solutions are of eikonal form, which has two roots and is typical for wave propagation. The scales $g_0$ and $g_1$ along with coefficients $A$ and $B$ can be expressed in closed form from (2.29) and (2.30). To accomplish this, the first scale $g_0$ can be solved. Hence the exponential factor may be examined as

$$\gamma(t_0) = \frac{-\bar{\zeta} \pm \sqrt{\bar{\zeta}^2 - 4\pi^2}}{2\pi\, g_0'(t_0)}. \tag{2.35}$$

To ensure a bounded solution, the derivative of $\gamma(t_0)$ must be zero (Nayfeh 2000). Therefore, the following ordinary differential equations (ODEs) are solved:

$$\gamma_1 = \frac{-\bar{\zeta} - \sqrt{\bar{\zeta}^2 - 4\pi^2}}{2\pi\, g_0'(t_0)}, \quad \gamma_2 = \frac{-\bar{\zeta} + \sqrt{\bar{\zeta}^2 - 4\pi^2}}{2\pi\, g_0'(t_0)}, \tag{2.36a,b}$$

where $\gamma_1$ and $\gamma_2$ are constants. The solutions for the scales can be written as

$$g_{0,1}(t_0) = -\frac{t_0\bar{\zeta}}{2\pi} - \frac{\sqrt{\bar{\zeta}^2 - 4\pi^2}}{2\pi}\, t_0, \quad g_{0,2}(t_0) = -\frac{t_0\bar{\zeta}}{2\pi} + \frac{\sqrt{\bar{\zeta}^2 - 4\pi^2}}{2\pi}\, t_0. \tag{2.37a,b}$$

To determine the conjugate functions $A$ and $B$, the terms corresponding to $\exp(\gamma_1 t_1)$ and $\exp(\gamma_2 t_1)$ are gathered and set to zero. Due to this constraint, singularities are suppressed, and two ODEs are obtained for $A$ and $B$:

$$\begin{aligned}&\frac{\mathrm{d}A}{\mathrm{d}t_0}\left(\bar{\zeta} + 2\pi\gamma_1 g_{0,1}'\right) + \left[\pi + \gamma_1 g_{0,1}'\left(\bar{\zeta} + \pi\gamma_1 g_{0,1}'\right)\right] C(t_0)\\ &\quad + \left\{2\pi\gamma_1^2 g_{0,1}' g_{1,1}' + \gamma_1\left[\zeta g_{1,1}' + \pi\left(g_{0,1}'\left(K\tau_1\,\varphi(x_f)\,\varphi'(x_f)\right) + g_{0,1}''\right)\right]\right\} A(t_0) = 0\end{aligned} \tag{2.38}$$

and

$$\begin{aligned}&\frac{\mathrm{d}B}{\mathrm{d}t_0}\left(\bar{\zeta} + 2\pi\gamma_2 g_{0,2}'\right) + \left[\pi + \gamma_2 g_{0,2}'\left(\bar{\zeta} + \pi\gamma_2 g_{0,2}'\right)\right] D(t_0)\\ &\quad + \left\{2\pi\gamma_2^2 g_{0,2}' g_{1,2}' + \gamma_2\left[\zeta g_{1,2}' + \pi\left(g_{0,2}'\left(K\tau_1\,\varphi(x_f)\,\varphi'(x_f)\right) + g_{0,2}''\right)\right]\right\} B(t_0) = 0.\end{aligned} \tag{2.39}$$

The solutions can be written as

$$\left.\begin{aligned} A(t_0) &= a_0 \exp\left(-\frac{1}{2} K t_0 \left(\frac{\bar{\zeta}}{\sqrt{\bar{\zeta}^2 - 4\pi^2}} + 1\right) \tau_1 \, \varphi(x_f) \, \varphi'(x_f) - g_{1,1}(t_0)\right), \\ B(t_0) &= b_0 \exp\left(\frac{1}{2} K t_0 \left(\frac{\bar{\zeta}}{\sqrt{\bar{\zeta}^2 - 4\pi^2}} - 1\right) \tau_1 \, \varphi(x_f) \, \varphi'(x_f) - g_{1,2}(t_0)\right). \end{aligned}\right\} \tag{2.40}$$

The first-order scale $g_1$ appears in both coefficients. The scale may be set to zero without loss of generality as it disappears from the expansion regardless of its value (Nayfeh 2000). The natural cancellation of this scale prevents interaction and overlapping scales with regard to $t_0$. From this specification, (2.29) and (2.30) are solved completely. The solution of (2.31) provides the coefficients $C$ and $D$, along with the slow scale $g_2$. First, the terms corresponding to $\exp(\gamma_1 t_1)$ and $\exp(\gamma_2 t_1)$ are gathered and set to zero to suppress any singularity behaviour. The ODE for $C$ is

$$\begin{aligned} &\frac{\mathrm{d}C}{\mathrm{d}t_0} + \frac{\{E(t_0)[\pi + \gamma_1 g'_{0,1}(\bar{\zeta} + \pi\gamma_1 g'_{0,1})] + \pi\gamma_1 \, C(t_0)[K\tau_1 \, \varphi(x_f) \, \varphi'(x_f) \, g'_{0,1} + g''_{0,1}]\}}{(\bar{\zeta} + 2\pi\gamma_1 g'_{0,1})} \\ &\quad - [a_0 K\pi \, \varphi(x_f) \, \varphi'(x_f)(\pi^2(4 + K\tau_1^2 \, \varphi(x_f) \, \varphi'(x_f)) - \bar{\zeta}^2) \\ &\quad - a_0\gamma_1(4\pi^2 - \bar{\zeta}^2)(\bar{\zeta} + 2\pi\gamma_1 g'_{0,1}) g'_{2,1}] \\ &\quad \times \frac{1}{(4\pi^2 - \bar{\zeta}^2)(\bar{\zeta} + 2\pi\gamma_1 g'_{0,1})} \exp\left(-\frac{1}{2} K t_0 \left(\frac{\bar{\zeta}}{\sqrt{\bar{\zeta}^2 - 4\pi^2}} + 1\right) \tau_1 \, \varphi(x_f) \, \varphi'(x_f)\right) = 0, \end{aligned} \tag{2.41}$$

with $D$ having a similar formulation. The solution can be written as

$$\begin{aligned} C(t_0) = c_0 &\exp\left(-\frac{1}{2} K t_0 \left(\frac{\bar{\zeta}}{\sqrt{\bar{\zeta}^2 - 4\pi^2}} + 1\right) \tau_1 \, \varphi(x_f) \, \varphi'(x_f)\right) \\ &+ \exp\left(-\frac{1}{2} K t_0 \left(\frac{\bar{\zeta}}{\sqrt{\bar{\zeta}^2 - 4\pi^2}} + 1\right) \tau_1 \, \varphi(x_f) \, \varphi'(x_f)\right) \\ &\times \left[\frac{a_0 K\pi \, \varphi(x_f) \, \varphi'(x_f) \left(\pi^2 \left(4 + K\tau_1^2 \, \varphi(x_f) \, \varphi'(x_f)\right) - \bar{\zeta}^2\right)}{\left(\bar{\zeta}^2 - 4\pi^2\right)^{3/2}} t_0 - a_0\gamma_1 g_{2,1}\right] \end{aligned} \tag{2.42}$$

and

$$\begin{aligned} D(t_0) = d_0 &\exp\left(\frac{1}{2} K t_0 \left(\frac{\bar{\zeta}}{\sqrt{\bar{\zeta}^2 - 4\pi^2}} - 1\right) \tau_1 \, \varphi(x_f) \, \varphi'(x_f)\right) \\ &+ \exp\left(\frac{1}{2} K t_0 \left(\frac{\bar{\zeta}}{\sqrt{\bar{\zeta}^2 - 4\pi^2}} - 1\right) \tau_1 \, \varphi(x_f) \, \varphi'(x_f)\right) \\ &\times \left[-\frac{b_0 K\pi \, \varphi(x_f) \, \varphi'(x_f)(\pi^2(4 + K\tau_1^2 \, \varphi(x_f) \, \varphi'(x_f)) - \bar{\zeta}^2)}{(\bar{\zeta}^2 - 4\pi^2)^{3/2}} t_0 - b_0\gamma_2 g_{2,2}\right]. \end{aligned} \tag{2.43}$$

The slow scale can be solved by eliminating the last part of the amplitude as

$$g_{2,1}(t_0) = \frac{K\pi\,\varphi(x_f)\,\varphi'(x_f)\left[4\pi^2 - \bar{\zeta}^2 + K\pi^2\tau_1^2\,\varphi(x_f)\,\varphi'(x_f)\right]}{\gamma_1\left(\bar{\zeta}^2 - 4\pi^2\right)^{3/2}}\,t_0, \tag{2.44}$$

$$g_{2,2}(t_0) = -\frac{K\pi\,\varphi(x_f)\,\varphi'(x_f)\left[4\pi^2 - \bar{\zeta}^2 + K\pi^2\tau_1^2\,\varphi(x_f)\,\varphi'(x_f)\right]}{\gamma_2\left(\bar{\zeta}^2 - 4\pi^2\right)^{3/2}}\,t_0. \tag{2.45}$$

The time scale of the first wave can be written as

$$\left.\begin{aligned} t_0 &= t, \\ t_1 &= -\frac{\omega t_0(\bar{\zeta} + \sqrt{\bar{\zeta}^2 - 4\pi^2})}{2\pi} \\ &\quad + \frac{K\pi\,\varphi(x_f)\,\varphi'(x_f)\left[4\pi^2 - \bar{\zeta}^2 + K\pi^2\tau_1^2\,\varphi(x_f)\,\varphi'(x_f)\right]}{\omega\left(\bar{\zeta}^2 - 4\pi^2\right)^{3/2}}\,t_0 + \cdots, \end{aligned}\right\} \tag{2.46}$$

while the time scale of the wave travelling in the opposite direction is

$$\left.\begin{aligned} t_0 &= t, \\ t_1 &= \frac{\omega t_0(-\bar{\zeta} + \sqrt{\bar{\zeta}^2 - 4\pi^2})}{2\pi} \\ &\quad - \frac{K\pi\,\varphi(x_f)\,\varphi'(x_f)\left[4\pi^2 - \bar{\zeta}^2 + K\pi^2\tau_1^2\,\varphi(x_f)\,\varphi'(x_f)\right]}{\omega\left(\bar{\zeta}^2 - 4\pi^2\right)^{3/2}}\,t_0 + \cdots. \end{aligned}\right\} \tag{2.47}$$

The terms $\gamma_1$ and $\gamma_2$ have been set to 1 without loss of generality. Such a time scale analysis can also be performed employing the Wentzel–Kramers–Brillouin (WKB) approach. The derivation of the solutions is demonstrated in Appendix A, showing and thereby verifying that the WKB approach scales align with the generalized scaling approach.

Several conclusions can be drawn from this solution and its respective scales. First, the solution takes the form of hyperbolic cosine and sine waves travelling in opposite directions, resembling the response of a damped oscillator. The heater power influences the amplitude of these waves. Additionally, factors such as time delay and acoustic intensity at the heater location contribute to the amplitude response. For the transient response, the damping primarily controls the fast oscillatory scale, while heat release, delay and acoustic intensity at the heater location influence the slower time scale.

### 2.3. *Method validation*

Figure 5 compares the theoretical Rijke tube data with the EVDP equation results. While minor phase lag deviations can be observed during the initial transient, the limit cycle prediction is reasonably accurate. The limit cycle amplitude, frequency, and the time required to reach the limit cycle agree well between the models. The statistical error of the EVDP system and the input system, the limit cycle amplitude and frequency, are chosen as the specific, quantifiable metrics, which are 1.4 % and 1.8 %, respectively, in figure 5.

Further validation is conducted on a modelled standing-wave thermoacoustic system with heat exchangers applied (aiming to create temperature gradient across the stack). The modelled systems consist of Navier–Stokes governing equations (PDEs). The modelled

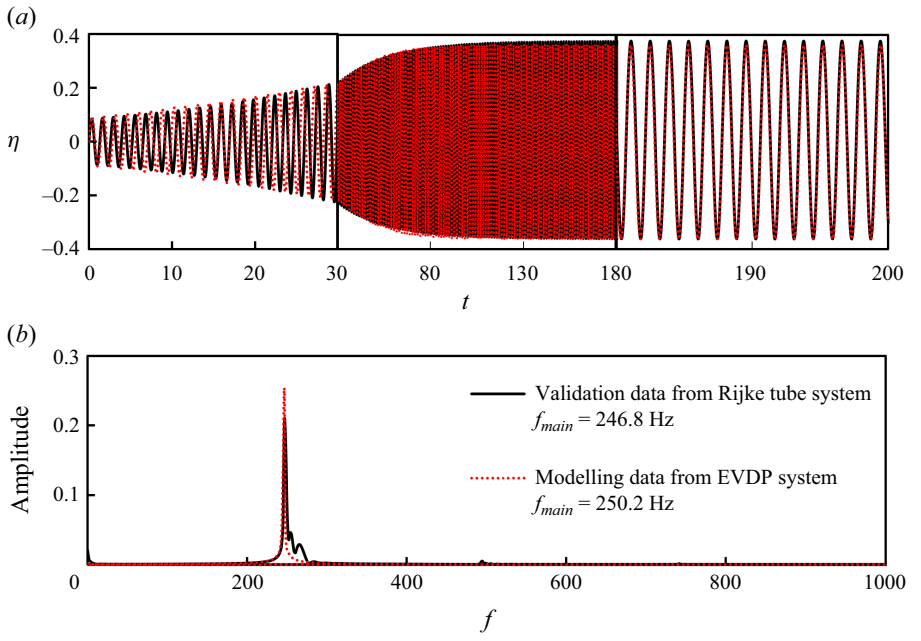


Figure 5. Comparison of the Rijke tube model and the EVDP model ($\mu_1 = 0.016$, $\mu_2 = 0.472$, $\mu_3 = 4.515$), for (*a*) oscillations and (*b*) frequency.

standing-wave TAE is three-dimensional. It is a simplified cylindrical tube with the left end rigidly closed (acoustic velocity node) and the right end open (acoustic pressure node). The TAE system is simulated numerically with standing $k$-$\epsilon$ of the WALE-LES turbulence model, and resolved in the computational fluid dynamics (CFD) solver ANSYS Fluent 19.0. More details like boundary conditions, computational settings (turbulence model) and validations can be found in previous work (Guo *et al.* 2023). The pressure fluctuations generated from the modelled TAE system are shown in figure 6(*a*). Before the limit cycle oscillations (LCOs) are generated, the flow disturbances decay rapidly first and then grow gradually. The decay behaviour is due to the initial energy dissipation. (The energy dissipates when pressure oscillation is not in phase with the unsteady heat release perturbations according to the Rayleigh criterion.) Therefore, the perturbations in the red circle (describing the rapid decay process) are neglected and deleted. The rest time series is non-dimensionalized to get the input data (figure 6*b*). After training the PINNs model, $\mu_1 = 0.0303$, $\mu_2 = 0.00648$ and $\mu_3 = 1.72$ are obtained. As shown in figures 6(*c*) and 6(*d*), the oscillations predicted from EVDP with variables obtained from PINNs fit well with the CFD model, and the error of the frequency and the limit cycle amplitude are 0.02 % and 0.05 %, respectively.

In general, the errors between these two data sets are acceptable. The validations of the two cases consisting of both ODE and PDE modelled thermoacoustic systems provide convincing evidence supporting the effectiveness and correctness of the proposed model to describe the nonlinear system reliably. Further investigations and comparisons can be conducted to examine the bifurcation characteristics of the coupled thermoacoustic systems.

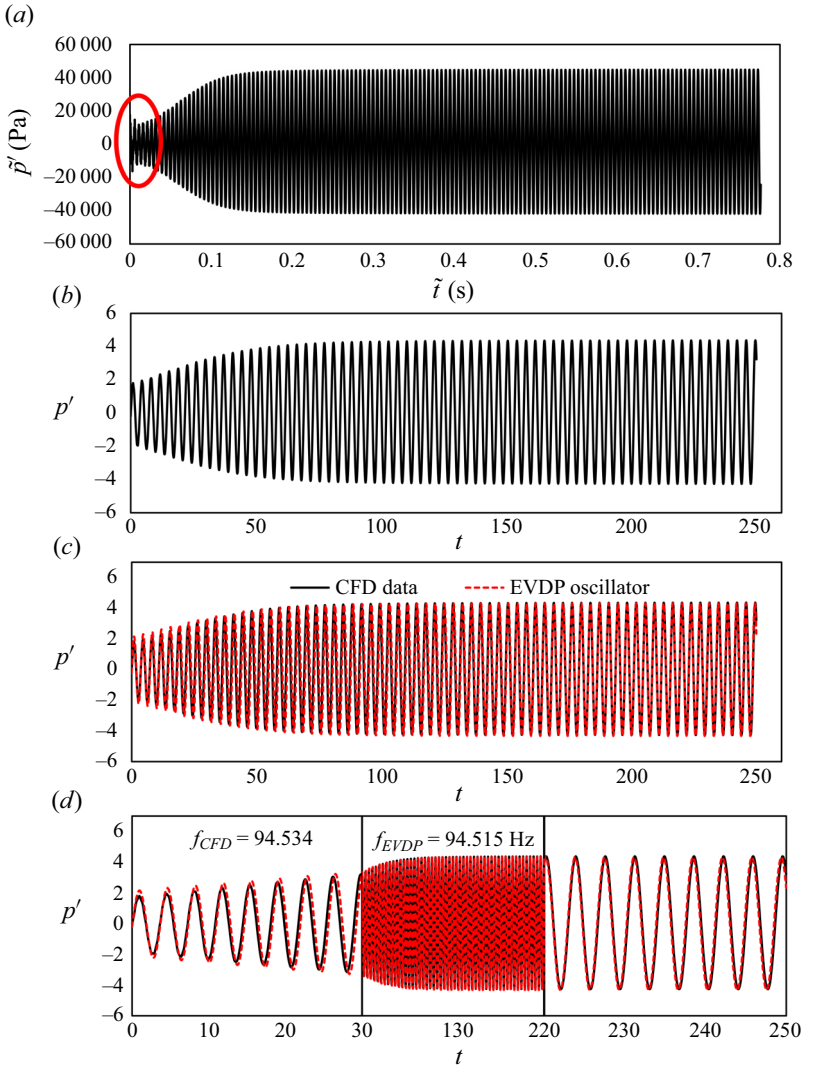


Figure 6. Validation of the PINNs-EVDP model with CFD data: (*a*) original data; (*b*) data processing; (*c*,*d*) comparison with the EVDP system.

## 3. Results

To illustrate the proposed model capabilities, the suppression of the hazardous thermoacoustic instability by the coupling method is demonstrated in this section. The amplitude reduction effect is verified in Appendix C based on the coupled simulation model mentioned before. Additionally, previous work (Biwa *et al.* 2015; Thomas *et al.* 2018; Ghosh, Mondal & Sujith 2022) showed that the governing equations describing the coupled dynamics of the thermoacoustic systems '*a*' and '*b*' can be expressed as

$$\frac{\mathrm{d}\dot{\eta}^a}{\mathrm{d}t} + \omega_a^2\eta^a + \zeta\dot{\eta}^a = \frac{\beta_a}{E_a}\varphi^a(x_f)\left\{\left|\frac{1}{3} - \varphi_n'(x_f)\,\eta^a(t-\tau_1)\right|^{1/2} - \left(\frac{1}{3}\right)^{1/2}\right\} + K_d(\dot{\eta}^b - \dot{\eta}^a) + K_\tau[\dot{\eta}^b(t-\tau_2) - \dot{\eta}^a(t)] \tag{3.1}$$

for coupled theoretical Rijke tubes, and

$$\frac{\mathrm{d}\dot{\eta}^a}{\mathrm{d}t} - \mu_1^a\mu_3^a\dot{\eta}^a + \mu_2^a\mu_3^a(\eta^a)^2\dot{\eta}^a + (\mu_3^a)^2\eta^a = K_d(\dot{\eta}^b - \dot{\eta}^a) + K_\tau[\dot{\eta}^b(t-\tau_2) - \dot{\eta}^a(t)] \tag{3.2}$$

for coupled EVDP systems (where the equations for the coupled thermoacoustic system $b$ can be obtained by alternating the superscripts). The coefficients $K_d$ and $K_\tau$ represent the strength of the dissipative and time-delay coupling effects, respectively, which could be controlled by a needle valve and a vinyl tube (Biwa *et al.* 2015). The dissipative coupling strength ($K_d$), detuning (the frequency ratio $R_\omega = \omega_1/\omega_2$), time-delay coupling strength ($K_\tau$) and time delay ($\tau_2$) are four control parameters that need to be determined. All ODEs are solved numerically by a fourth-order Runge–Kutta scheme.

### 3.1. *Effect of time-delay coupling*

Due to the time required for a signal to travel from one system to another, the coupling process involves time delays. The time-delay coupling effects are illustrated in figure 7, based on the oscillator located on the right-hand side of the Hopf point (which can be seen in figure 4*a*) without considering dissipative coupling and detuning. The bifurcation curves shown in figure 7(*d*), delineating the parameter plane into regions of AD and LCO, exhibit a consistent pattern for both coupled systems at small time delays. The one-parameter bifurcation diagrams plotted in figures 7(*a*) and 7(*c*) reveal a small discrepancy in point $A$ with $K_\tau = 0.2$ and $\tau_2 = 0.2$. The coupled oscillation is depicted in figure 8(*a*) and demonstrates a faster decay towards AD in the theoretical, coupled Rijke tube systems compared to the coupled EVDP systems. The oscillation amplitude in the EVDP systems decreases more slowly, but AD will be reached when sufficient simulation time is provided. In conclusion, the coupled systems based on the proposed EVDP approach can accurately predict the time-delay coupling effects when the time delay is smaller than the central point. The central point, identified as the point around which the AD occurs most efficiently, is found to be near $\omega\tau_2 = 0.815\pi$ in the current study. The central point was found to be $\omega\tau_2 = \pi$ in Thomas *et al.* (2018), and $\omega\tau_2 = \pi/2$ in Biwa *et al.* (2015). The amplitude reduction may be attributed to the negative feedback resulting from self-sustained oscillations and phase-lagged oscillations of the feedback signal (Thomas *et al.* 2018).

Upon passing the central point, the differences in the predictions become evident. Figure 7(*b*) shows that the EVDP systems require a smaller time-delay coupling strength to achieve AD at large time delays ($\tau_2 > 0.7$). At point $B$ (as shown in figure 8*b*), the coupled EVDP systems decay to AD, while the theoretical, coupled Rijke tube systems experience a decrease in amplitude before settling into a low-amplitude steady state. This observation suggests that the theoretical and dynamic differences between these two systems are not the same. Comparing (2.2) and (2.22), using the EVDP equation as the alternative system, transfers the nonlinearity from the source term to the damping term, which makes the strong nonlinear system a weaker nonlinear system. Due to this transfer of nonlinearity, the bifurcation difference is unavoidable. Therefore, when time delay $\tau_2$, which influences the nonlinearity of the system, is small, the differences of the AD region are small, while when time delay $\tau_2$ increases, the difference is intensified as shown in figure 7(*d*). This divergence of AD results in the coupled proposed alternative system exhibiting a slightly wider AD region. Hence the proposed method will be more reliable with a small $\tau_2$

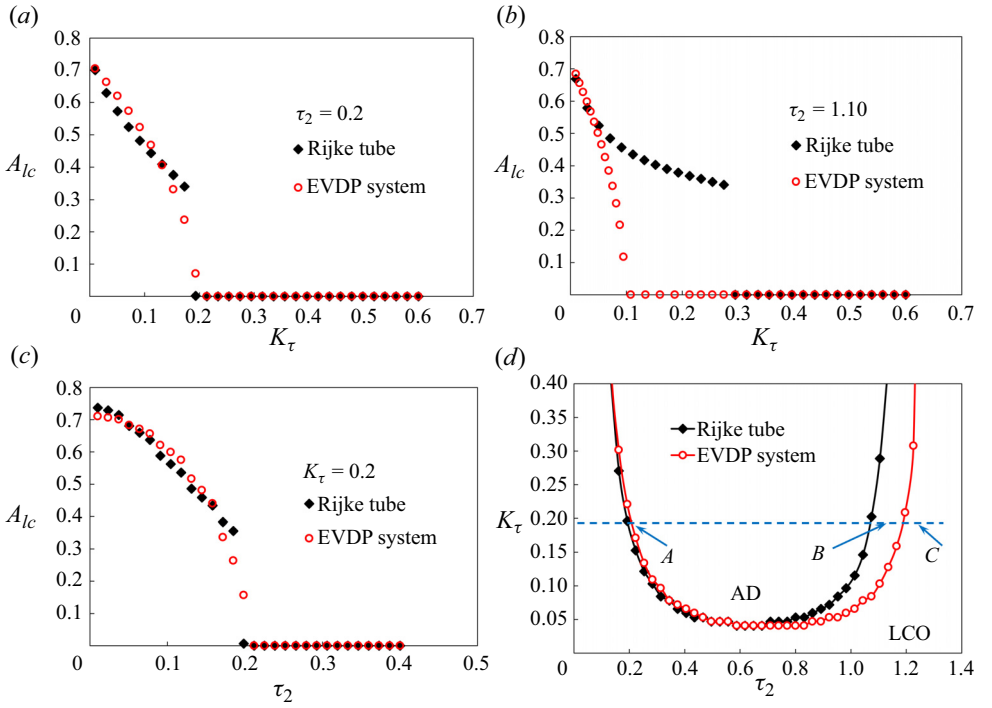


Figure 7. Effects of coupling strength ($K_\tau$) and time delay ($\tau_2$) in the coupling Rijke tube system and the EVDP system symbolized by the amplitude of the end cycle. (No dissipative coupling and detuning effects with $K_d = 0$ and $R_\omega = 1$.) One-parameter bifurcation diagrams with (*a*) $\tau_2 = 0.2$, (*b*) $\tau_2 = 1.1$, (*c*) $K_\tau = 0.2$. (*d*) Two-parameter bifurcation diagram in the parameter plane. The points A, B, C in figure 7(*d*) are correspondingly plotted in the time domains in figure 8(*a*), (*b*) and (*c*), respectively. Here, $A_{lc}$ represents the amplitude of the limit cycle when it is stabilized.

value for a controller strategy, when using the alternative EVDP system to determine the coupling parameters.

### 3.2. *Effect of dissipative coupling*

To investigate the impact of dissipative coupling, two non-identical Rijke tubes (with natural frequency ratio $R_\omega = 0.878$) are designed with the theoretical model for coupling by adjusting the temperature gradient across the heat source. The temporal perturbations are then used to learn the proposed EVDP model. Figure 9 shows the model results when weak and strong dissipative coupling effects are applied without time-delay coupling ($K_\tau = 0$). The coupled EVDP oscillators exhibit almost identical behaviour regardless of the dissipative coupling strength. For low dissipative coupling strength, the oscillators settle into a low-amplitude LCO state. The coupled oscillation amplitudes exhibit periodic variations attributed to the weak interaction effects between the coupled oscillators with close but unequal natural frequencies. The oscillation amplitudes diminish to AD with sufficiently high dissipative coupling strength ($K_d = 0.18$ in figure 9*b*).

One-parameter bifurcation plots, shown in figure 10, illustrate the effect of the natural frequency ratios on the oscillation amplitudes. The coupled oscillators exhibit LCO behaviour only when the frequency ratio is close to 1, regardless of the coupling strength. Hence the theoretical Rijke tube and EVDP systems need substantial natural frequency

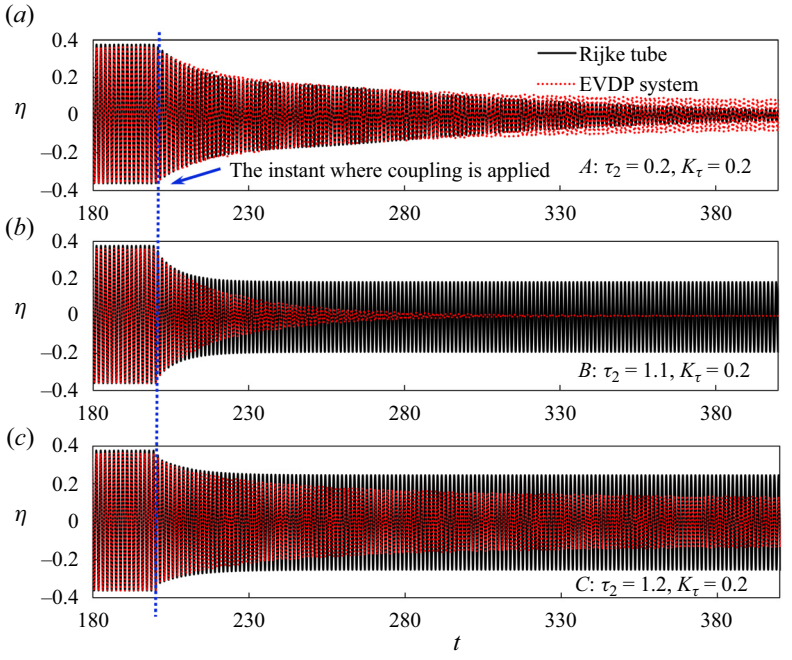


Figure 8. Coupling oscillations of the coupling systems at the following points: (*a*) *A* with $\tau_2 = 0.2$ and $K_\tau = 0.2$; (*b*) *B* with $\tau_2 = 1.1$ and $K_\tau = 0.2$; (*c*) *C* with $\tau_2 = 1.2$ and $K_\tau = 0.2$.

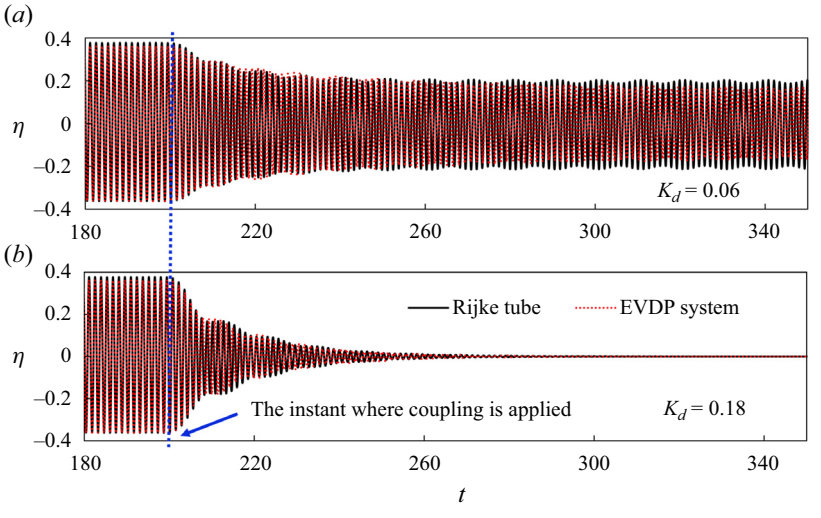


Figure 9. Coupling oscillations when the dissipative coupling is applied: (*a*) weak dissipative coupling; (*b*) strong dissipative coupling. For these cases, $K_\tau = 0$ and $R_\omega = 0.878$.

differences to approach AD states. The bifurcation characteristics of these two systems are similar, but the EVDP system predicts wider AD regions.

The two-parameter bifurcation diagram for the theoretical, coupled Rijke tube systems is plotted in figure 11(*a*) to explain the change of the AD region with increasing $K_d$. The blue areas represent the AD phenomenon, i.e. the limit cycle amplitude approaches zero.

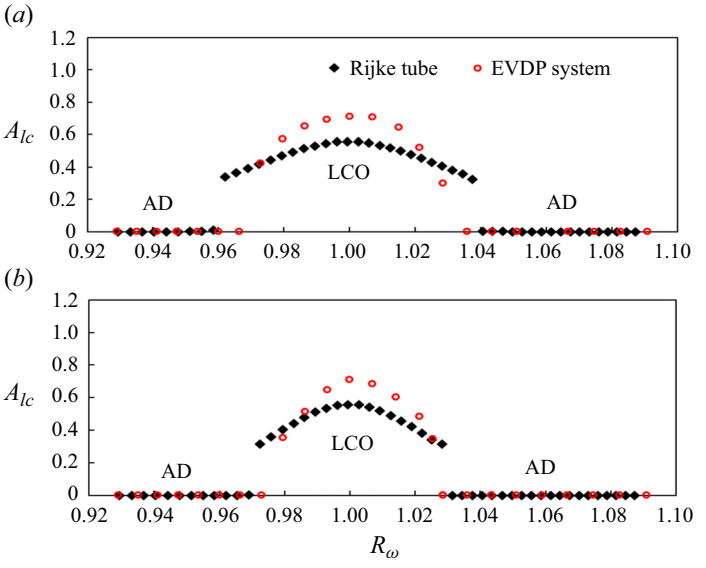


Figure 10. One-parameter bifurcation diagrams varying the natural frequency ratio, where $K_\tau = 0$: (*a*) $K_d = 0.10$, and (*b*) $K_d = 0.18$.

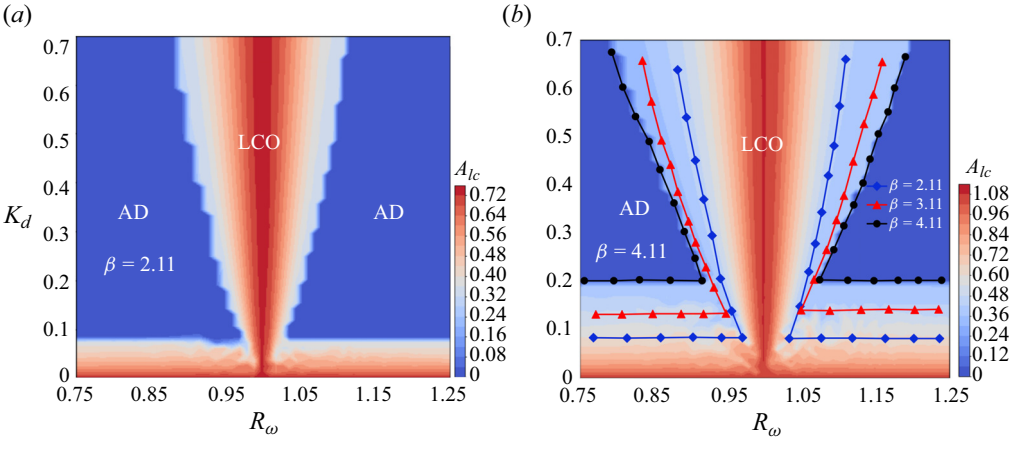


Figure 11. Two-parameter bifurcation diagram with varying $R_\omega$ and $K_d$ for the Rijke tube system for (*a*) $\beta = 2.11$, (*b*) $\beta = 4.11$, with the bifurcation curves plotted for different $\beta$ values.

The system cannot approach AD regardless of the detuning strength until the dissipative strength of the coupling reaches a 0.083 bifurcation value. At this critical point, an important region of AD emerges suddenly. The AD region gradually decreases as the dissipative strength continues increasing beyond this point. This is consistent with the results shown in figure 10. Biwa *et al.* (2015) also reported that the oscillation amplitudes controlled by the heater power value ($\beta$) impacted the coupling. Hence diagrams with different $\beta$ values are presented in figure 11(*b*), showing that higher heater power values require higher dissipative coupling or detuning strength to attain AD. Thus a rising $\beta$ value amplifies the limit cycle amplitude and reduces the AD region.

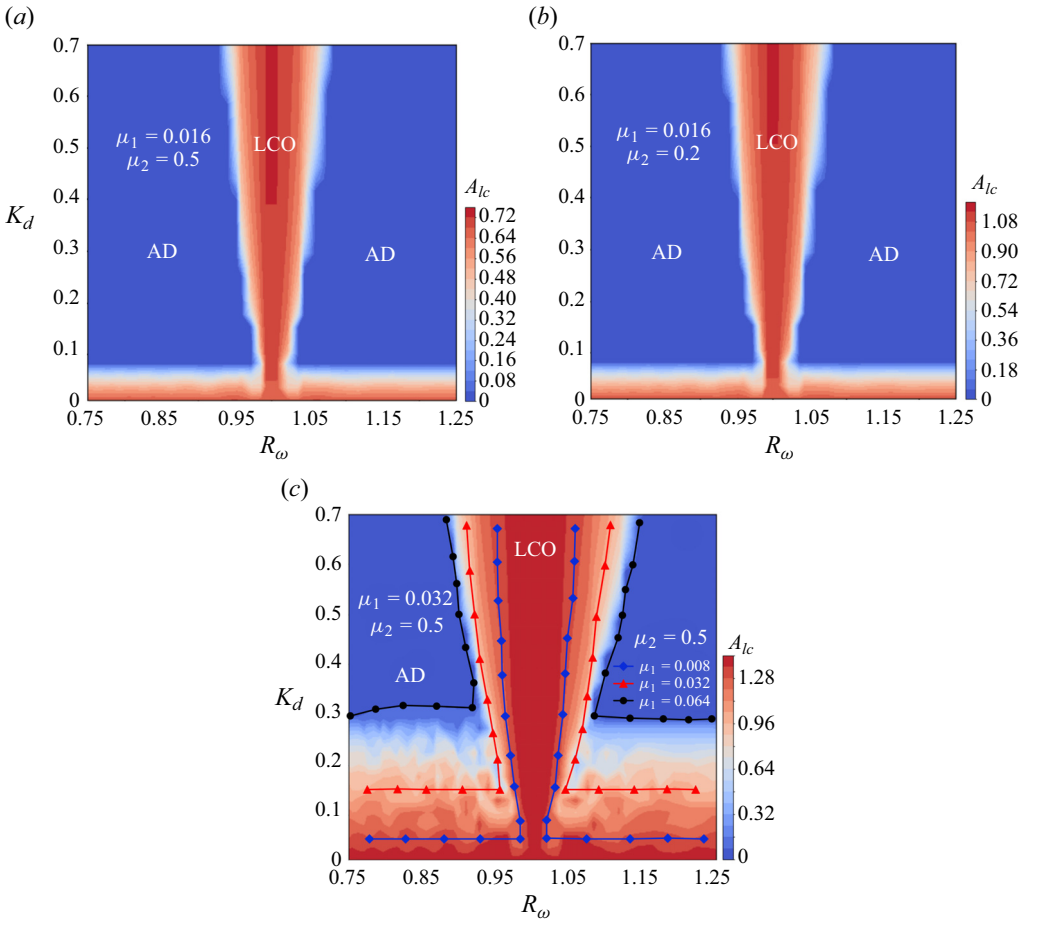


Figure 12. Two-parameter bifurcation diagram illustrating variations in $R_\omega$ and $K_d$ for the EVDP system ($\mu_3 = 4.5$), for (*a*) $\mu_1 = 0.016$, $\mu_2 = 0.5$, (*b*) $\mu_1 = 0.016$, $\mu_2 = 0.2$, (*c*) $\mu_1 = 0.032$, $\mu_2 = 0.5$, with the bifurcation curves plotted for different $\mu_1$ values.

The two-parameter bifurcation analysis is also carried out for the coupled EVDP systems. Figure 12(*a*) reveals that the two-parameter plane is divided into two distinct regions resembling the pattern observed in figure 11. Comparing figures 12(*a*) and 12(*b*) (where $\mu_2$ is decreased and $\mu_1$ is equal) reveals only a minor amplitude decrease with an unchanged bifurcation boundary. Hence $\mu_2$ damps the oscillation amplitude, and changes of $\mu_2$ have negligible effects on the dissipative coupling. However, changing the $\mu_1$ value causes a distinct behaviour, as shown in figure 12(*c*) (where $\mu_2$ is held constant and $\mu_1$ is increased). Here, $\mu_1$ and $\beta$ have similar properties, i.e. higher parameter values increase the limit cycle amplitude and extend the LCO region. These observations suggest that the parameter $\mu_1$ in the EVDP model mimics the heating power $\beta$ in the theoretical Rijke-type thermoacoustics system. Thus, the EVDP equation can be rearranged such that the 'source' term with coefficient $\mu_1$ is on the right-hand side of the equation:

$$\ddot{\psi} + \mu_2\mu_3\psi^2\dot{\psi} + \mu_3^2\psi = \mu_1\mu_3\dot{\psi}. \tag{3.3}$$

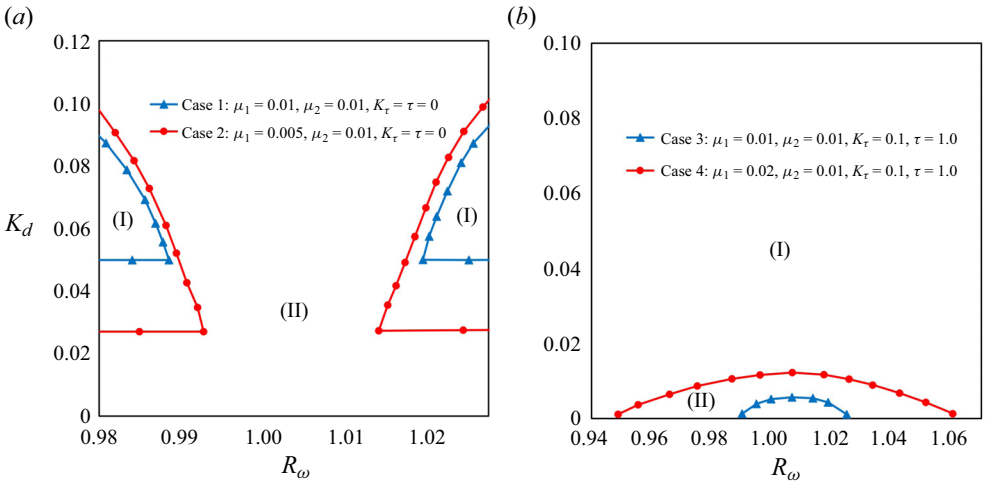


Figure 13. Theoretically predicted bifurcation diagrams from our coupled EVDP oscillators ($\mu_3 = 4.5$). Regions (I) and (II) denote high-amplitude oscillation and AD, respectively.

The EVDP equation can be interpreted physically. Based on (2.10), the amplitude of the EVDP system is facilitated by raising $\mu_1$ and decreasing $\mu_2$, while according to Euler's formula, the real part of the exponent influences the amplitude of the oscillation, and the imaginary part determines the frequency of the function. Therefore, based on the results (2.40) and (2.46) from such a generalized scaling method, the amplitude of $\eta$ is influenced by the heating power (enhancing it) and damping (diminishing it), which is consistent with the results obtained from (2.10) as shown in figure 2. According to the comparison of the two-parameter bifurcation diagram, the variable $\mu_1$ contributes the same efforts of the heating power to the Rijke tube system, and the variable $\mu_2$ corresponds to the damping term, which have the same contributions to the amplitude of coupled EVDP systems. More accurately, the rising $\mu_1$ enhances the oscillations and leads to the same type of AD boundary, while the increasing $\mu_2$ diminishes the amplitude, which is visually evident from figure 12(*a*) with figure 12(*b*). Thus we can draw the physical relevance of these variables and get the one-to-one correspondence between (2.20) and (2.2) from the EVDP system to the Rijke-type thermoacoustic system: the coefficient term $\mu_2$ represents the system damping, the coefficient term $\mu_3$ integrates the frequency information of the thermoacoustic system, and the coefficient term $\mu_1$ can be regarded as the source term of the system, representing the instability intensity introduced by the nonlinear heat source.

As for the oscillations observed from the single TAE system, the coupling bifurcation characteristics for the coupled EVDP systems need to be further validated based on either experimental tests or numerical simulations. As reported in previous work (Biwa *et al.* 2015), the classical VDP system can reproduce the experimental systems. Therefore, the bifurcation investigation of coupled EVDP systems is conducted and shown in figure 13. As depicted in figure 13, cases 1 and 2 are coupled solely by the dissipative coupling, while cases 3 and 4 involve both the dissipative and time-delay couplings. Additionally, cases 1 and 3 represent the EVDP system (when $\mu_1 = \mu_2$), and cases 2 and 4 represent the EVDP system (when $\mu_1 \neq \mu_2$). In other words, the EVDP system has the potential to replicate the experimental thermoacoustic system, although the hydrodynamic equations governing thermoacoustic oscillators are far more complicated. Selecting a proper EVDP system

to be the alternative system for the system identification is appropriate for the coupling method as discussed in the present work.

Looking forward, while the EVDP system effectively captures the stable periodic solution oscillation or coupling bifurcation, it lacks the subcritical bifurcation features as observed in the Rijke tube system depicted in figure 4 due to its singular bifurcation point ($\mu_1 = 0$). Additionally, the conversion of such nonlinearity from the source term to the damping term results in a weakened nonlinearity, leading to non-negligible differences in the AD region for coupled systems. Consequently, there is potential to explore better alternative systems for enhancing the PINNs model to yield the characters above. For instance, based on the PINNs model, one may utilize the classical VDP oscillator with a forcing term, the Rijke tube theoretical model, or incorporate multiple modes; all of which may aid in capturing the subcritical bifurcation characteristics of uncoupled system and the AD characteristics of the coupled system. This exploration could significantly enhance the predictive capabilities and further advance our understanding of such complex nonlinear dynamics related to the large-amplitude thermoacoustic instability.

## 4. Discussion and conclusions

We proposed an approach to find descriptions of the instability behaviour of thermoacoustic systems by exact PDEs, which can be utilized for control strategy analysis. Therefore, the van der Pol (VDP) equation was reformulated, and the unknown parameters were determined using PINNs to solve the inverse problems. The proposed extended VDP (EVDP) model was validated in terms of oscillation and bifurcation characteristics against CFD data of a thermoacoustic engine (TAE) system and a horizontal Rijke tube modelled by the Galerkin series with the modified King's law. Further, the system coupling effect was explored, and control parameters were derived for coupled Rijke tube systems and the coupled EVDP systems. The main findings can be summarized as follows.

(1) The reformulated, nonlinear VDP equation with fitted coefficients by the PINN approach was shown to be capable of replicating the thermoacoustic system instability behaviour. The frequency, limit cycle amplitude, and the time required to reach the limit cycle of the Rijke tube system and the CFD simulation TAE system were predicted accurately. The validation provides evidence for the method's ability to obtain reliable alternative deterministic system descriptions.

(2) The coupled system becomes more prone to AD near a central point with varying time-delay coupling strength. The coupled EVDP systems exhibit almost identical bifurcation characteristics to the coupled Rijke tube system for short time delays on the left-hand side of the central point. For larger time delays, the nonlinear differences between the two systems are amplified, leading to a wider region of AD for the coupled EVDP systems. The differences are unavoidable due to the nonlinearity shift from the source term to the damping term when the EVDP system is used as the alternative system.

(3) The coupled EVDP systems and the coupled Rijke tube systems can attain AD, when the dissipative coupling strength reaches sufficiently high levels or when the natural frequency differences between the coupled systems are significant. As the coupling strength increases, the AD region emerges at specific bifurcation values and diminishes subsequently.

(4) The variable $\mu_1$ was shown to affect the two-parameter bifurcation character similarly as the heater power parameter $\beta$, which supports assigning the EVDP model physical significance. The terms with coefficients $\mu_1$, $\mu_2$ and $\mu_3$ can be

interpreted as source term, damping term, and term containing the frequency information, respectively.

**Acknowledgements.** The authors appreciate the reviewers and the editor for their careful reading and many constructive comments and suggestions on improving the manuscript. The first author would like to acknowledge that the present research was conducted under the supervision of Professor D. Zhao during her CSC-sponsored visit to University of Canterbury in 2023. Dr L. Guo conducted CFD simulations on coupled TAE (standing-wave thermoacoustic engines) systems

**Funding.** The first author is grateful for the financial support from the Scholarship Council (grant no. 202206130055) for providing scholarship to enable the author to study at the University of Canterbury. This research work is jointly sponsored by the University of Canterbury (grant no.452DISDZ), the National Natural Science Foundation of China (no. 51876056) and Hunan Provincial Innovation Foundation for Postgraduate (no. CX20200413). X.Z. and D.Z. would like to thank the Faculty of Engineering for their financial and computing support.

**Declaration of interests.** The authors report no conflict of interest.

**Author ORCIDs.**
Xinyu Zhao https://orcid.org/0009-0002-0862-964X;
Dan Zhao https://orcid.org/0000-0002-4484-6505;
Cody Shelton https://orcid.org/0000-0001-7996-2816;
Bernhard Semlitsch https://orcid.org/0000-0001-7715-863X.

**Author contributions.** M.X. wrote the original draft. M.X. processed and analysed the research results and discussed with D.Z., X.Z. and C.S., D.Z. conceived and initialized the project. All authors contributed to the paper writing and English editing. All authors have contributed to the manuscript.

## Appendix A. The WKB approach

In order to verify the results from the generalized scaling method, the WKB approximation is carried out. First, the solution $\eta$ is assumed to have the exponential form

$$\eta = \exp\left(\frac{S_0(t)}{\varepsilon} + S_1(t) + \varepsilon\, S_2(t) + \cdots\right). \tag{A1}$$

The derivatives may be derived easily as

$$\eta' = \left(\frac{S_0'(t)}{\varepsilon} + S_1'(t) + \varepsilon\, S_2'(t) + \cdots\right)\eta \tag{A2}$$

and

$$\eta'' = \left[\left(\frac{S_0''(t)}{\varepsilon} + S_1''(t) + \varepsilon\, S_2''(t) + \cdots\right) + \left(\frac{S_0'(t)}{\varepsilon} + S_1'(t) + \varepsilon\, S_2'(t) + \cdots\right)^2\right]\eta. \tag{A3}$$

Inserting these expressions into (2.24), a series of three ordinary equations may be derived. The first equation, corresponding to the fast variations in the wave propagation, is the eikonal equation, which is very similar to the equation derived in the generalized scaling method. The next equation is the transport equation, controlling mainly the amplitude of oscillations. Finally, the slow scale $S_2$ may be resolved. Mathematically, these equations

may be written as

$$\left(\frac{\mathrm{d}S_0}{\mathrm{d}t}\right)^2 + \frac{\bar{\zeta}}{\pi} v \frac{\mathrm{d}S_0}{\mathrm{d}t} + 1 = 0, \tag{A4}$$

with

$$\frac{\bar{\zeta}}{\pi}\frac{\mathrm{d}S_1}{\mathrm{d}t} + 2\frac{\mathrm{d}S_0}{\mathrm{d}t}\frac{\mathrm{d}S_1}{\mathrm{d}t} + K\varphi(x_f)\varphi'(x_f)\tau_1\frac{\mathrm{d}S_0}{\mathrm{d}t} + \frac{\mathrm{d}^2S_0}{\mathrm{d}t^2} = 0 \tag{A5}$$

and

$$\frac{\bar{\zeta}}{\pi}\frac{\mathrm{d}S_2}{\mathrm{d}t} + 2\frac{\mathrm{d}S_0}{\mathrm{d}t}\frac{\mathrm{d}S_2}{\mathrm{d}t} + K\varphi(x_f)\varphi'(x_f)\left(\tau_1\frac{\mathrm{d}S_1}{\mathrm{d}t} - 1\right) + \left(\frac{\mathrm{d}S_1}{\mathrm{d}t}\right)^2 + \frac{\mathrm{d}^2S_1}{\mathrm{d}t^2} = 0. \tag{A6}$$

For the purposes of verifying the generalized scaling method, initial conditions will not be applied in order to compare the results. First, (A4) may be solved, which is both nonlinear and quadratic with respect to the scale $S_0$. This matches the same physical explanation given in the generalized scaling method where two waves are moving in opposite directions. The solution may be written as

$$S_{0,1} = -\frac{\bar{\zeta}}{2\pi}t - \frac{\sqrt{\bar{\zeta}^2 - 4\pi^2}}{2\pi}t, \quad S_{0,2} = -\frac{\bar{\zeta}}{2\pi}t + \frac{\sqrt{\bar{\zeta}^2 - 4\pi^2}}{2\pi}t, \tag{A7a,b}$$

which reveals the same scales achieved earlier, $S_0 = g_0$. Next, (A5) is solved for $S_1$ and may be described as

$$\left.\begin{aligned} S_{1,1} &= -\frac{1}{2}Kt\left(\frac{\bar{\zeta}}{\sqrt{\bar{\zeta}^2 - 4\pi^2}} + 1\right)\tau_1\varphi(x_f)\varphi'(x_f), \\ S_{1,2} &= \frac{1}{2}Kt\left(\frac{\bar{\zeta}}{\sqrt{\bar{\zeta}^2 - 4\pi^2}} - 1\right)\tau_1\varphi(x_f)\varphi'(x_f), \end{aligned}\right\} \tag{A8}$$

which corresponds to the exponential argument presented in (2.40). Finally, the scale $S_2$ may be written as

$$\left.\begin{aligned} S_{2,1} &= \frac{K\pi\varphi(x_f)\varphi'(x_f)\left[4\pi^2 - \bar{\zeta}^2 + K\pi^2\tau_1^2\varphi(x_f)\varphi'(x_f)\right]}{\left(\bar{\zeta}^2 - 4\pi^2\right)^{3/2}}t, \\ S_{2,2} &= -\frac{K\pi\varphi(x_f)\varphi'(x_f)\left[4\pi^2 - \bar{\zeta}^2 + K\pi^2\tau_1^2\varphi(x_f)\varphi'(x_f)\right]}{\left(\bar{\zeta}^2 - 4\pi^2\right)^{3/2}}t, \end{aligned}\right\} \tag{A9}$$

which is equal to (2.45), i.e. $S_2 = g_2$. In conclusion, the WKB approach scales align with the generalized scaling approach.

## Appendix B. Parameters and corresponding values for the modelled system

The critical parameters used in the modelled Rijke tube system in figure 5 in § 2.3 are summarized in table 1.

| Parameter | Symbol | Value |
|---|---|---|
| Mean inlet temperature | $T_1$ | 300 |
| Heater power | $\beta$ | 2.11 |
| Tube length | $L$ | 1 |
| Mean temperature gradient | $T_2/T_1$ | 2.8 |
| Heat source time delay | $\tau$ | 0.02 |
| Damping parameter 1 | $\zeta_1$ | 0.03 |
| Damping parameter 2 | $\zeta_2$ | 0.003 |

Table 1. Critical parameters of the dimensionless variable for the modelled Rijke tube system.

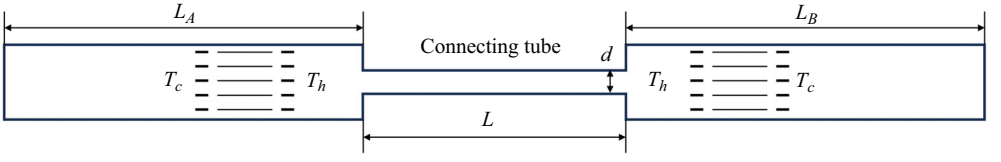


Figure 14. Numerically modelled coupled TAE (standing-wave thermoacoustic engines) systems based on previous experiments (Hyodo & Biwa 2019) in the presence of a connecting tube. Here, $L_A = 860$ mm, $L_B = 920$ mm, $T_c = 300$ K, $T_h = 425$ K, $L = 800$ mm, $d = 80$ mm.

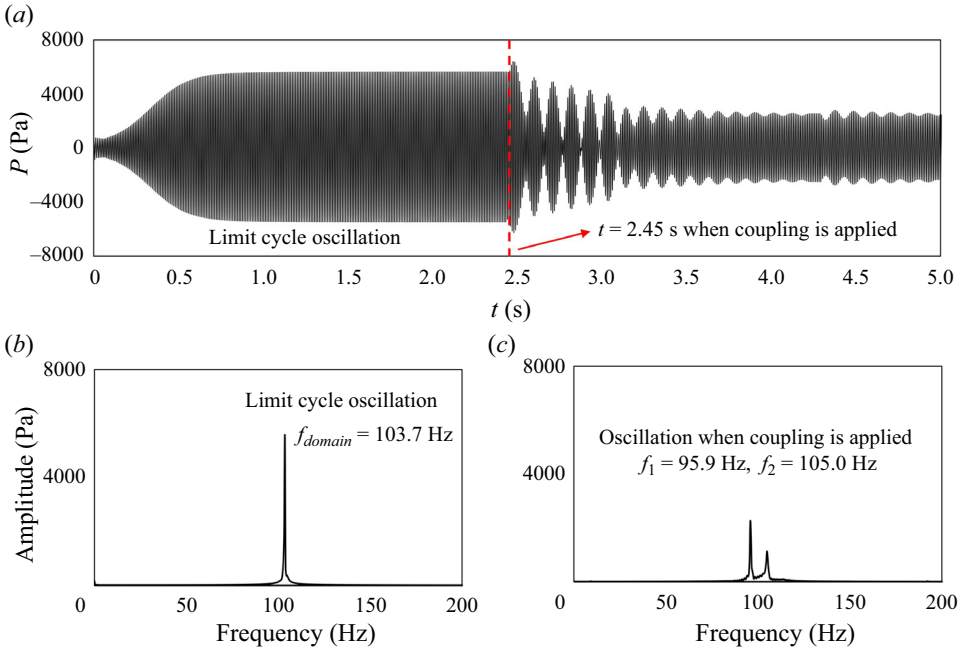


Figure 15. Our CFD simulation results of amplitude reduction for the coupled TAE systems via the connecting tube: (*a*) time evolution of pressure before and after coupling; (*b*) pressure spectra before coupling; (*c*) pressure spectra after coupling at $t = 2.45$ s.

## Appendix C. Verification of the amplitude suppression effect on the coupling method based on the CFD simulation model

Two numerically modelled TAE systems are coupled by a connecting tube in our CFD simulations, as shown in figure 14. This is an effective coupling method as validated

in previous experiments (Hyodo & Biwa 2019). The numerically predicted amplitude reduction from the modelled TAE systems is observed when $L = 800$ mm, $d = 80$ mm, as depicted in figure 15. The pressure perturbations are attenuated from LCOs with amplitude 5800 Pa to oscillations with maximum amplitude 2900 Pa via a beating behaviour. Correspondingly, the pressure spectra as shown in the frequency domain reveal that the perturbations with a single dominant frequency at 103.7 Hz are changed to those with two dominant frequencies at 95.9 Hz and 105.0 Hz, with a much lower amplitude. All this confirms that the amplitude reduction could be achieved in the modelled coupled TAE systems.

## References


Aliakbari, M, Soltany Sadrabadi, M., Vadasz, P. & Arzani, A. 2023 Ensemble physics informed neural networks: a framework to improve inverse transport modeling in heterogeneous domains. *Phys. Fluids* **35** (5), 053616.

Backhaus, S. & Swift, G.W. 1999 A thermoacoustic Stirling heat engine. *Nature* **399** (6734), 335–338.

Balasubramanian, K. & Sujith, R.I. 2008 Thermoacoustic instability in a Rijke tube: non-normality and nonlinearity. *Phys. Fluids* **20** (4), 044103.

Balusamy, S., Li, L.K.B., Han, Z., Juniper, M.P. & Hochgreb, S. 2015 Nonlinear dynamics of a self-excited thermoacoustic system subjected to acoustic forcing. *Proc. Combust. Inst.* **35** (3), 3229–3236.

Biwa, T., Sawada, Y., Hyodo, H. & Kato, S. 2016 Suppression of spontaneous gas oscillations by acoustic self-feedback. *Phys. Rev. Appl.* **6** (4), 044020.

Biwa, T., Tozuka, S. & Yazaki, T. 2015 Amplitude death in coupled thermoacoustic oscillators. *Phys. Rev. Appl.* **3** (3), 034006.

Bonciolini, G., Faure-Beaulieu, A., Bourquard, C. & Noiray, N. 2021 Low order modelling of thermoacoustic instabilities and intermittency: flame response delay and nonlinearity. *Combust. Flame* **226**, 396–411.

Bragg, S.L. 1964 Noise and oscillations in jet engines (substance of a Friday evening discourse delivered before the Royal Institution on November 15). *Nature* **201**, 123–129.

Cai, S., Mao, Z., Wang, Z., Yin, M. & Karniadakis, G.E. 2021 Physics-informed neural networks (PINNs) for fluid mechanics: a review. *Acta Mechanica Sin.* **37** (12), 1727–1738.

Dowling, A.P. 1995 The calculation of thermoacoustic oscillations. *J. Sound Vib.* **180** (4), 557–581.

Dowling, A.P. & Morgans, A.S. 2005 Feedback control of combustion oscillations. *Annu. Rev. Fluid Mech.* **37**, 151–182.

Ghosh, A., Mondal, S. & Sujith, R.I. 2022 Occasional coupling enhances amplitude death in delay-coupled oscillators. *Chaos* **32** (10), 101106.

Guan, Y., Li, L.K.B., Jegal, H. & Kim, K.T. 2023 Effect of flame response asymmetries on the modal patterns and collective states of a can-annular lean-premixed combustion system. *Proc. Combust. Inst.* **39** (4), 4731–4739.

Guan, Y., Moon, K., Kim, K.T. & Li, L.K.B. 2021 Low-order modeling of the mutual synchronization between two turbulent thermoacoustic oscillators. *Phys. Rev.* E **104** (2), 024216.

Guo, L., Zhao, D., Xu, J., Tokhi, M.O. & Karimi, H.R. 2023 Predicting unsteady heat–fluid interaction features and nonlinear acoustic behaviors in standing-wave thermoacoustic engines using unsteady RANS, LES and hybrid URANS/LES methods. *Intl Commun. Heat Mass Transfer* **142**, 106617.

Heckl, M.A. 1990 Non-linear acoustic effects in the Rijke tube. *Acta Acust.* **72** (1), 63–71.

Hyodo, H. & Biwa, T. 2019 Amplitude death in coupled thermoacoustic oscillators with frequency detuning. In *Proceedings of the 23rd International Congress on Acoustics, Sept. 9–23, Aachen*, pp. 5627–5632. Deutsche Gesellschaft für Akustik e.V. (DEGA).

Juniper, M.P. 2011 Triggering in the horizontal Rijke tube: non-normality, transient growth and bypass transition. *J. Fluid Mech.* **667**, 272–308.

Juniper, M.P. & Sujith, R.I. 2018 Sensitivity and nonlinearity of thermoacoustic oscillations. *Annu. Rev. Fluid Mech.* **50**, 661–689.

Karniadakis, G.E., Kevrekidis, I.G., Lu, L., Perdikaris, P., Wang, S. & Yang, L. 2021 Physics-informed machine learning. *Nat. Rev. Phys.* **3** (6), 422–440.

KRYLOV, N.M. & BOGOLYUBOV, N.N. 1947 *Introduction to Non-Linear Mechanics*. Princeton University Press.

LI, S., LI, Q., TANG, L., YANG, B., FU, J., CLARKE, C.A., JIN, X., JI, C.Z. & ZHAO, H. 2016*a* Theoretical and experimental demonstration of minimizing self-excited thermoacoustic oscillations by applying anti-sound technique. *Appl. Energy* **181**, 399–407.

LI, X., ZHAO, D., YANG, X., WEN, H., JIN, X., LI, S., ZHAO, H., XIE, C. & LIU, H. 2016*b* Transient growth of acoustical energy associated with mitigating thermoacoustic oscillations. *Appl. Energy* **169**, 481–490.

LIU, Y., CHENG, L. & DU, J. 2022 Multi-modal thermoacoustic instability suppression via locally resonant and Bragg bandgaps. *J. Acoust. Soc. Am.* **152** (6), 3471–3482.

LIU, Y., LIU, P., WANG, Z., AO, W. & GUAN, Y. 2023 Large eddy simulation of combustion instability in a subcritical hydrogen peroxide/kerosene liquid rocket engine: intermittency route to period-2 thermoacoustic instability. *Phys. Fluids* **35** (6), 065145.

LU, L., MENG, X., MAO, Z. & KARNIADAKIS, G.E. 2021 DeepXDE: a deep learning library for solving differential equations. *SIAM Rev.* **63** (1), 208–228.

LYU, Z., FANG, Y. & WANG, G. 2023 Precursor detection of thermoacoustic instability using statistical complexity and artificial neural network. *Phys. Fluids* **35** (6), 064101.

MARIAPPAN, S., NATH, K. & KARNIADAKIS, G.E. 2023 Learning thermoacoustic interactions in combustors using a physics-informed neural network. arXiv:2401.00061.

MCMANUS, K.R., POINSOT, T. & CANDEL, S.M. 1993 A review of active control of combustion instabilities. *Prog. Energy Combust. Sci.* **19** (1), 1–29.

NAGARAJA, S., KEDIA, K. & SUJITH, R.I. 2009 Characterizing energy growth during combustion instabilities: singularvalues or eigenvalues? *Proc. Combust. Inst.* **32** (2), 2933–2940.

NAJI, S., RAHIMI, A., BAZARGAN, V. & MARENGO, M. 2023 Numerical and artificial neural network analysis of an axisymmetric co-flow-focusing microfluidic droplet generator using active and passive control. *Phys. Fluids* **35** (6), 062008.

NAYFEH, A.H. 2000 *Perturbation Methods*. Wiley.

NBENDJO, B.R.N. & YAMAPI, R. 2007 Active control of extended van der Pol equation. *Commun. Nonlinear Sci. Numer. Simul.* **12** (8), 1550–1559.

OZAN, D.E. & MAGRI, L. 2023 Physics-aware learning of nonlinear limit cycles and adjoint limit cycles. In *INTER-NOISE and NOISE-CON Congress and Conference Proceedings* (ed. B.M. Gibbs), vol. 265, pp. 1191–1199. Institute of Noise Control Engineering.

PERKO, L. 2013 *Differential Equations and Dynamical Systems*, 3rd edn. Springer Science & Business Media.

RAISSI, M., PERDIKARIS, P. & KARNIADAKIS, G.E. 2017*a* Physics informed deep learning (part I): data-driven solutions of nonlinear partial differential equations. arXiv:abs/1711.10561.

RAISSI, M., PERDIKARIS, P. & KARNIADAKIS, G.E. 2017*b* Physics informed deep learning (part II): data-driven discovery of nonlinear partial differential equations. arXiv:abs/1711.10566.

RAUN, R.L., BECKSTEAD, M.W., FINLINSON, J.C. & BROOKS, K.P. 1993 A review of Rijke tubes, Rijke burners and related devices. *Prog. Energy Combust. Sci.* **19** (4), 313–364.

RAYLEIGH, LORD 1878 The explanation of certain acoustical phenomena. *Nature* **18**, 319–321.

SAHAY, A., ROY, A., PAWAR, S.A. & SUJITH, R.I. 2021 Dynamics of coupled thermoacoustic oscillators under asymmetric forcing. *Phys. Rev. Appl.* **15** (4), 044011.

SRIKANTH, S., SAHAY, A., PAWAR, S.A., MANOJ, K. & SUJITH, R.I. 2022 Self-coupling: an effective method to mitigate thermoacoustic instability. *Nonlinear Dyn.* **110** (3), 2247–2261.

SU, J., YANG, D. & MORGANS, A.S. 2022 Low-frequency acoustic radiation from a flanged circular pipe at an inclined angle. *J. Acoust. Soc. Am.* **151** (2), 1142–1157.

SUBRAMANIAN, P., SUJITH, R.I. & WAHI, P. 2013 Subcritical bifurcation and bistability in thermoacoustic systems. *J. Fluid Mech.* **715**, 210–238.

SUJITH, R.I. & UNNI, V.R. 2020 Complex system approach to investigate and mitigate thermoacoustic instability in turbulent combustors. *Phys. Fluids* **32** (6), 061401.

SUN, Y., ZHAO, D., JI, C., ZHU, T., RAO, Z. & WANG, B. 2022 Large-eddy simulations of self-excited thermoacoustic instability in a premixed swirling combustor with an outlet nozzle. *Phys. Fluids* **34** (4), 044112.

THOMAS, N., MONDAL, S., PAWAR, S.A. & SUJITH, R.I. 2018 Effect of time-delay and dissipative coupling on amplitude death in coupled thermoacoustic oscillators. *Chaos* **28** (3), 033119.

VINOD, V. & BALARAM, B. 2023 On the spatial spread of active control in a van der Pol ring via synchronisation and its stabilisation using parameter mismatch. *Commun. Nonlinear Sci. Numer. Simul.* **117**, 106944.

WANG, X., WEN, H., HU, T. & WANG, B. 2023 Flow-field reconstruction in rotating detonation combustor based on physics-informed neural network. *Phys. Fluids* **35** (7), 076109.

WU, G., XU, X., LI, S. & JI, C. 2019 Experimental studies of mitigating premixed flame-excited thermoacoustic oscillations in T-shaped combustor using an electrical heater. *Energy* **174**, 1276–1282.

WU, J., NAN, J., YANG, L. & LI, J. 2023 Reconstruction of the flame nonlinear response using deep learning algorithms. *Phys. Fluids* **35** (1), 017125.

XU, S., YAN, C., ZHANG, G., SUN, Z., HUANG, R., JU, S., GUO, D. & YANG, G. 2023 Spatiotemporal parallel physics-informed neural networks: a framework to solve inverse problems in fluid mechanics. *Phys. Fluids* **35** (6), 065141.

YAMAPI, R., NANA NBENDJO, B.R. & ENJIEU KADJI, H.G. 2007 Dynamics and active control of motion of a driven multi-limit-cycle van der Pol oscillator. *Intl J. Bifurcation Chaos* **17** (04), 1343–1354.

YANG, L., PANG, B. & LI, J. 2021 Comparison of strongly and weakly nonlinear flame models applied to thermoacoustic instability. *Phys. Fluids* **33** (9), 094108.

YAZDANI, A., LU, L., RAISSI, M. & KARNIADAKIS, G.E. 2020 Systems biology informed deep learning for inferring parameters and hidden dynamics. *PLoS Comput. Biol.* **16** (11), e1007575.

YU, J., LU, L., MENG, X. & KARNIADAKIS, G.E. 2022 Gradient-enhanced physics-informed neural networks for forward and inverse PDE problems. *Comput. Meth. Appl. Mech. Engng* **393**, 114823.

ZHANG, C., TAO, C., SONG, H., HAN, X., LI, L., LIU, X. & QI, F. 2023 Experimental investigations on central vortex core in swirl spray flames using high-speed laser diagnostics. *Phys. Fluids* **35** (3), 035130.

ZHANG, M., LI, J., CHENG, W. & LI, T. 2020 Active control of thermoacoustic instability using microsecond plasma discharge. *J. Appl. Phys.* **127** (3), 033301.

ZHAO, D. 2012 Transient growth of flow disturbances in triggering a Rijke tube combustion instability. *Combust. Flame.* **159** (6), 2126–2137.

ZHAO, D. 2023*a* Chapter 6 – active control of thermoacoustic instability. In *Thermoacoustic Combustion Instability Control* (ed. D. Zhao), pp. 443–512. Academic.

ZHAO, D. 2023*b* Chapter 7 – passive control of combustion instabilities. In *Thermoacoustic Combustion Instability Control* (ed. D. Zhao), pp. 513–583. Academic.

ZHAO, D., JI, C., LI, X. & LI, S. 2015 Mitigation of premixed flame-sustained thermoacoustic oscillations using an electrical heater. *Intl J. Heat Mass Transfer* **86**, 309–318.

ZHAO, D. & LI, X.Y. 2015 A review of acoustic dampers applied to combustion chambers in aerospace industry. *Prog. Aerosp. Sci.* **74**, 114–130.

ZHAO, D. & MORGANS, A.S. 2009 Tuned passive control of combustion instabilities using multiple Helmholtz resonators. *J. Sound Vib.* **320** (4–5), 744–757.

ZHAO, D. & REYHANOGLU, M. 2014 Feedback control of acoustic disturbance transient growth in triggering thermoacoustic instability. *J. Sound Vib.* **333** (16), 3639–3656.

ZHAO, X., ZHAO, D., CHENG, L., SHELTON, C.M. & MAJDALANI, J. 2023 Predicting thermoacoustic stability characteristics of longitudinal combustors using different endpoint conditions with a low Mach number flow. *Phys. Fluids* **35** (9), 094122.